SANDIA REPORT
SAND2022-2750 Rev. 1
Printed April 2022

Sandia National Laboratories

MELCOR Accident Progression and Source Term Demonstration Calculations for HTGR

Kenneth Wagner
Bradley Beeny
David Luxat

Prepared by
Sandia National Laboratories
Albuquerque, New Mexico
87185 and Livermore,
California 94550

Issued by Sandia National Laboratories, operated for the United States Department of Energy by National Technology & Engineering Solutions of Sandia, LLC.

Available to DOE and DOE contractors from
U.S. Department of Energy
Office of Scientific and Technical Information
P.O. Box 62
Oak Ridge, TN 37831

Telephone: (865) 576-8401
Facsimile: (865) 576-5728
E-Mail: reports@osti.gov
Online ordering: http://www.osti.gov/scitech

Available to the public from
U.S. Department of Commerce
National Technical Information Service
5301 Shawnee Rd
Alexandria, VA 22312

Telephone: (800) 553-6847
Facsimile: (703) 605-6900
E-Mail: orders@ntis.gov
Online order: https://classic.ntis.gov/help/order-methods/

ABSTRACT

MELCOR is an integrated thermal hydraulics, accident progression, and source term code for reactor safety analysis that has been developed at Sandia National Laboratories for the United States Nuclear Regulatory Commission (NRC) since the early 1980s. Though MELCOR originated as a light water reactor (LWR) code, development and modernization efforts over the past decades have expanded its application scope to include non-LWR reactor concepts. Current MELCOR development efforts include providing the NRC with the analytical capabilities to support regulatory readiness for licensing non-LWR technologies under Strategy 2 of the NRC's near-term Implementation Action Plans. Beginning with the Next Generation Nuclear Project (NGNP), MELCOR has undergone a range of enhancements to provide analytical capabilities for modeling the spectrum of advanced non-LWR concepts. This report describes the generic plant model developed to demonstrate MELCOR capabilities to perform high-temperature gas reactor (HTGR) safety evaluations. The generic plant model is based on publicly available PMBR-400 design information. For plant aspects (e.g., reactor building size and leak rate) that are not described in the PBMR-400 references, the analysts made assumptions needed to construct a MELCOR full-plant model. The HTGR model uses a TRi-structural ISOtropic (TRISO)-particle fuel pebble-bed reactor with a primary system rejecting heat to a recuperative heat exchanger. Surrounding the reactor vessel is a reactor cavity contained within a confinement room cooled by the Reactor Cavity Cooling System (RCCS). Example calculations are performed to show the plant response and MELCOR capabilities to characterize a range of accident conditions. The accidents selected for evaluation consider a range of degraded and failed modes of operation for key safety functions providing reactivity control, primary system heat removal and reactor vessel decay heat removal, and confinement cooling.

ACKNOWLEDGEMENTS

This work was funded by the NRC as part of the development and demonstration activities defined in the NRC Non-Light Water Reactor Vision and Strategy Volume 3: Computer Code Development Plans for Severe Accident Progression, Source Term, and Consequence Analysis [1]. The authors gratefully acknowledge the contributions from Jason Schaperow, Hossein Esmaili, and Don Algama of the US NRC for their valuable technical guidance.

Dr. David Louie provided valuable support on developing the containment model, the reactor cavity cooling system, and the preliminary radionuclide release modeling input parameters for the PBMR-400 demonstration model. Fred Gelbard provided fundamental research and guidance on the radionuclide behavior.

Dr. Steve Skutnik of Oak Ridge National Laboratories performed the PBMR-400 SCALE analysis and provided the radionuclide decay heat power, radionuclide inventory, and the core axial and radial power profile for this analysis. The documentation of their analysis is in ORNL/TM-2020/1886, "Assessment of ORIGEN Reactor Library Development for Pebble-Bed Reactors Based on the PBMR-400 Benchmark," July 2021 and is part of the same NRC-sponsored effort.

CONTENTS

1. INTRODUCTION 1
2. MELCOR HTGR Modeling Features 3
2.1. MELCOR HTGR-specific Models 3
2.2. MELCOR HTGR Solution Methodology 4
3. MODEL DESCRIPTION 6
3.1. PBMR-400 Model Nodalization 6
3.1.1. Reactor Vessel Nodalization 6
3.1.2. Primary and Secondary System Nodalization 14
3.1.3. Confinement and Reactor Cavity Cooling System Nodalization 15
3.2. Radionuclide Inventory and Decay Heat Input 18
3.3. Fission Production Release 20
3.4. Point Kinetics Modeling 25
3.5. Steady State Initialization 25
4. EXAMPLE RESULTS 29
4.1. Depressurized Loss-of-Forced Circulation 29
4.2. Depressurized Loss-of-Forced Circulation Sensitivity Study 38
4.3. Anticipated Transient Without SCRAM 48
5. SUMMARY 51
Appendix A. Cesium Diffusion During Normal Operations 54

LIST OF FIGURES

Figure 2-1 MELCOR PBMR radionuclide release models. 4
Figure 2-2 MELCOR HTGR solution methodology 5
Figure 3-1 PBMR-400 reactor vessel [9]. 7
Figure 3-2 PBMR-400 COR nodalization. 11
Figure 3-3 PBMR-400 radial cross-section [9]. 12
Figure 3-4 PBMR-400 vessel CVH and FL nodalization. 13
Figure 3-5 PBMR-400 primary and secondary CVH and FL nodalization during the steady state 14
Figure 3-6 PBMR-400 primary and secondary CVH and FL nodalization during the DLOFC scenario after the hot leg pipe break 15
Figure 3-7 PBMR-400 confinement CVH and FL nodalization with NGNP schematic [10] 17
Figure 3-8 Example of an airflow RCCS [12] 18

Figure 3-9 PBMR-400 decay heat curve. 20
Figure 3-10 MELCOR intact TRISO model [19]. 22
Figure 3-11 TRISO fuel failure fraction curve. 24
Figure 3-12 NGPN reactivity feedback curves [21]. 25
Figure 3-13 Steady state core inlet pressure comparison to the OECD benchmark. 26
Figure 3-14 Steady state core inlet and outlet temperature comparison to the OECD benchmark. 27
Figure 3-15 Steady state core pressure drop comparison to the OECD benchmark. 27
Figure 3-16 Steady state vessel flow comparison to the OECD benchmark. 28
Figure 3-17 Steady state core power. 28
Figure 4-1 Vessel inlet pressure response. 30
Figure 4-2 Flows in and out of the broken piping 31
Figure 4-3 Flowrates in the core 31
Figure 4-4 Fuel temperature profile in the inner region of the core. 32
Figure 4-5 Comparison of decay heat and oxidation power. 33
Figure 4-6 Carbon-monoxide and carbon-dioxide production. 34
Figure 4-7 Carbon-monoxide and carbon-dioxide mole fractions in the reactor building. 34
Figure 4-8 Iodine release and distribution. 36
Figure 4-9 Cesium release and distribution 36
Figure 4-10 TRISO failure fraction and peak fuel temperature 37
Figure 4-11 Distribution of the released iodine and cesium distribution in the base case. 38
Figure 4-12 Uncertain parameter impact on the peak fuel temperature 43
Figure 4-13 Uncertain parameter impact on the TRISO failure fraction. 43
Figure 4-14 Uncertain parameter impact on the iodine release from the pebbles. 44
Figure 4-15 Uncertain parameter impact on the cesium from the pebbles. 44
Figure 4-16 Uncertain parameter impact on the iodine release to the environment. 45
Figure 4-17 Uncertain parameter impact on the cesium release to the environment. 45
Figure 4-18 Reactor building uncertain parameter impact on the iodine release to the environment. 46
Figure 4-19 Reactor building uncertain parameter impact on the cesium release to the environment. 46
Figure 4-20 Comparison of the base case and blocked RCCS oxidation gases. 47
Figure 4-21 Comparison of the base case and blocked RCCS reactor building carbon monoxide mole fraction. 47

Figure 4-22 Core power and RCCS response in the ATWS. 49
Figure 4-23 Average Doppler, moderator, and xenon feedback in the ATWS. 49
Figure 4-24 Average fuel and reflector feedback in the ATWS. 50
Figure 4-25 Average TRISO fraction in the ATWS. 50

LIST OF TABLES

Table 3-1 Key parameters for the PBMR-400 [9]. 8
Table 3-2. Typical building coefficients [14]. 16
Table 3-3 MELCOR radionuclide classes 19
Table 3-4 PBMR-400 radionuclide class masses 19
Table 3-5 Diffusivities used in the PBMR-400 model [16] 23
Table 3-6 CORSOR-Booth radionuclide release scaling factors [8]. 23
Table 3-7 MELCOR radionuclide classes [8]. 24
Table 4-1 Uncertain parameters for the PBMR-400. 42

This page left blank

ACRONYMS AND DEFINITIONS

Abbreviation	Definition
ATWS	Anticipated Transient without SCRAM
BWR	Boiling Water Reactor
COR	Core
CV	Control Volume
CVH	Control Volume Hydrodynamics
DLOFC	Depressurized Loss-of-Forced Circulation
DOE	United State Department of Energy
FL	Flow Path
FU	Fuel
HGTR	High-Temperature Gas Reactor
IAEA	International Atomic Energy Agency
LWR	Light Water Reactor
MST	Mechanistic Source Term
MX	Matrix
NEA	Nuclear Energy Agency
NGNP	Next Generation Nuclear Plant
NRC	United States Nuclear Regulatory Commission
OECD	Organization of Economic and Cooperative Development
ORNL	Oak Ridge National Laboratory
PBMR	Pebble Bed Modular Reactor
PLOFC	Pressurized Loss-of-Forced Circulation
RCCS	Reactor Cavity Cooling System
RF	Reflector
RN	Radionuclide
SBO	Station Blackout
SS	Stainless steel
TAMU	Texas A&M University
TRISO	TRi-structural ISOtropic particle fuel

1. INTRODUCTION

MELCOR is an integrated systems-level thermal hydraulics and source term code for reactor safety analysis [1]. It has been developed at Sandia National Laboratories for the United States Nuclear Regulatory Commission (NRC) since the early 1980s. Current MELCOR development efforts include providing the NRC with the accident analysis capabilities to support regulatory readiness for licensing non-light water reactor (non-LWR) technologies under Strategy 2 of the NRC's near-term Implementation Action Plans [2]. Beginning with the Department of Energy (DOE) Next Generation Nuclear Project (NGNP), MELCOR has undergone a range of enhancements to provide analytical capabilities for modeling the spectrum of advanced non-LWR concepts. A detailed description of the development process, including identification of technical gaps, is provided in NRC's "Non-Light Water Reactor (Non-LWR) Vision and Strategy, Volume 3 – Computer Code Development Plans for Severe Accident Progression, Source Term, and Consequence Analysis" (NRC ADAMS Accession No. ML20030A178). This report describes the generic MELCOR plant model developed to demonstrate MELCOR capabilities to perform high-temperature gas-cooled reactor (HTGR) safety evaluations.

The MELCOR HTGR model is applied to provide an example of a mechanistic source term (MST) analysis. The scope of MST demonstration project includes development and application of a MELCOR full-plant model using publicly-available references and data. The project also includes MST demonstration calculations for other non-LWR designs that will be documented in separate reports (e.g., a heat pipe reactor and a molten-salt-cooled pebble-bed reactor).

MELCOR characterizes the evolution of the accident from the early thermal-hydraulic response through the core heat up, including the release and transport of radionuclides from the primary system to the containment or confinement buildings and the environment. The code is a knowledge repository from decades of experiments and model development with a historical focus on LWR phenomenology. However, MELCOR has been extended over the past decade with new models to address non-LWR technologies.

MELCOR relies on the SCALE code system to provide the radionuclide inventories, kinetics parameters, power distributions, and decay heat, especially through the ORIGEN code. SCALE is a multi-disciplinary tool developed by Oak Ridge National Laboratory for the NRC to combine nuclear system simulation tools into one cohesive package [3]. SCALE provides a comprehensive, verified and validated, user-friendly tool set for nuclear data, criticality safety, reactor physics, radiation shielding, radioactive source term characterization, activation, depletion and decay, and sensitivity and uncertainty analysis under a software quality assurance program. Since the 1970s, regulators, licensees, and research institutions around the world have used SCALE for safety analysis.

The MELCOR HTGR input model used for the MST analysis is based on a pebble bed modular reactor (PBMR) model developed at Texas A&M University (TAMU) [4]. The current scope of work included (a) an update of the input model to the current version of the MELCOR code, (b) incorporation of the SCALE inventory, axial and radial power profile decay heat tables, (c) incorporation of TRISO fission product release models, (d) a confinement building, (e) the passive reactor cavity cooling system, and (f) radionuclide tracking algorithms. Section 2 describes the PBMR model used in the MST calculation.

The PBMR MELCOR plant model is used to simulate a depressurized loss-of-forced circulation (DLOFC) scenario. The development of the input model identified gaps and uncertainties in design

input data. Consequently, sensitivity calculations were performed to illustrate the relative magnitude in key figures of merit due to variations in the selected uncertainty parameters. The DLOFC accident progression and the source term results are described in Section 4. A summary is presented in Section 5.

This report describes the MELCOR HTGR full-plant deck and its application to select scenarios. In addition, this work was presented at a public workshop on July 20, 2021. The video recording and presentation material are available at the following links:

- Video – https://youtu.be/I_7GIOeXVtw
- Slides – SCALE MELCOR HTGR slides ML21200A179 [5]

2. MELCOR HTGR MODELING FEATURES

The MELCOR code is organized into "packages" that correspond to different groupings of reactor regions, physics, or other code functionalities. The balance of the plant is modeled using the building block components of control volumes, heat structures, and flow paths. These basic components are used to represent primary system, the reactor vessel, the reactor building or containment, and the secondary system, which will be described for the HTGR demo model in the next section. These fundamental modeling features are used for all reactor types. A unique capability of MELCOR includes an integrated calculation of radionuclide release, transport, and deposition in any problem description or nodalization. The level of modeling detail or discretization is user-specified based on the objectives of the analysis. An example for the Pebble Bed Modular Reactor 400 (PBMR-400) is described in this report, which was used in an OECD benchmark study [6]. The next subsections describe some of the key MELCOR models used in the PBMR-400 demo calculations and an overview of the calculation solution methodology.

2.1. MELCOR HTGR-specific Models

Superimposed in the reactor core portion of the vessel nodalization are special models for pebble bed and prismatic HTGR fuel modeling. The fuel description and associated physics are modeled in the "COR" package. The PBMR-400 COR modeling includes representation of the reflectors, the pebbles containing the TRISO fuel, and the TRISO fuel. The MELCOR HTGR COR package calculates the thermal response of the pebbles, the surrounding reflectors, the reactor fission power response (i.e., a point kinetics model), and the radionuclide release [8].

The MELCOR HTGR COR package diffusional fission product release model calculates the radionuclide distribution and transport within the TRISO and pebbles. Any radionuclides reaching the surface of the pebble are released to MELCOR's Control Volume Hydrodynamic (CVH) Package and tracked in the Radionuclide (RN) Package for the subsequent transport and deposition. The COR package also calculates the radionuclide behavior during normal power operation. The scope of the modeling includes the amount (and species) of radionuclides generated in the fuel kernels (i.e., as specified by amounts provided by the SCALE code), the amount recoiled and diffused to the buffer layer, the amount diffused into or through the dense coating layers, the amount released from the kernels of particles with failed coating layers, and the amount which diffuses through the graphite pebble matrix (see Figure 2-1). A detailed description of the TRISO radionuclide behavior models is presented in Reference [8].

The MELCOR HTGR COR package models the combined radiation and conduction heat transfer within the pebble bed. The special heat transfer model accounts for radiation and conduction through a packed bed (i.e., the Zehner-Schlunder-Bauer model with the Breitbach-Barthels modification to the radiation term [8]). The combined radiation and conduction model also predicts the radial and axial heat transfer to the surrounding reflectors. The pebble bed convective heat transfer model accounts for natural or forced convective heat transfer from a sphere as flow conditions evolve during the transient. The flow resistance through the pebble bed is based on an Achenbach modification to the porous bed flow resistance [8].

Postulated accident conditions in a HTGR can lead to the ingression of air or steam into the core. Consequently, the COR package includes steam and air oxidation models. The steam oxidation correlation calculates the rate of oxidation as a function of the partial pressure of the steam and hydrogen adjacent to the graphite using a parabolic kinetics formulation. Similarly, the air oxidation model calculates the rate of oxidation as a function of the partial pressure of the oxygen adjacent to the graphite. Both the steam and air oxidation correlations include a rate limit due to steam or

oxygen diffusion towards the graphite surface. The chemical equilibrium of reaction products is assumed using correlations for the relative extent of reactions producing carbon-monoxide gas versus carbon-dioxide gas.

Finally, MELCOR includes a point kinetics model for the core power evaluation during a transient. The kinetics equations are a function of the reactor's thermal power and the thermal power generated by the 6 groups of delayed-neutron precursors. The model includes generalized interfaces for reactivity feedbacks from the fuel, the moderator, the control rods, and the neutron sources.

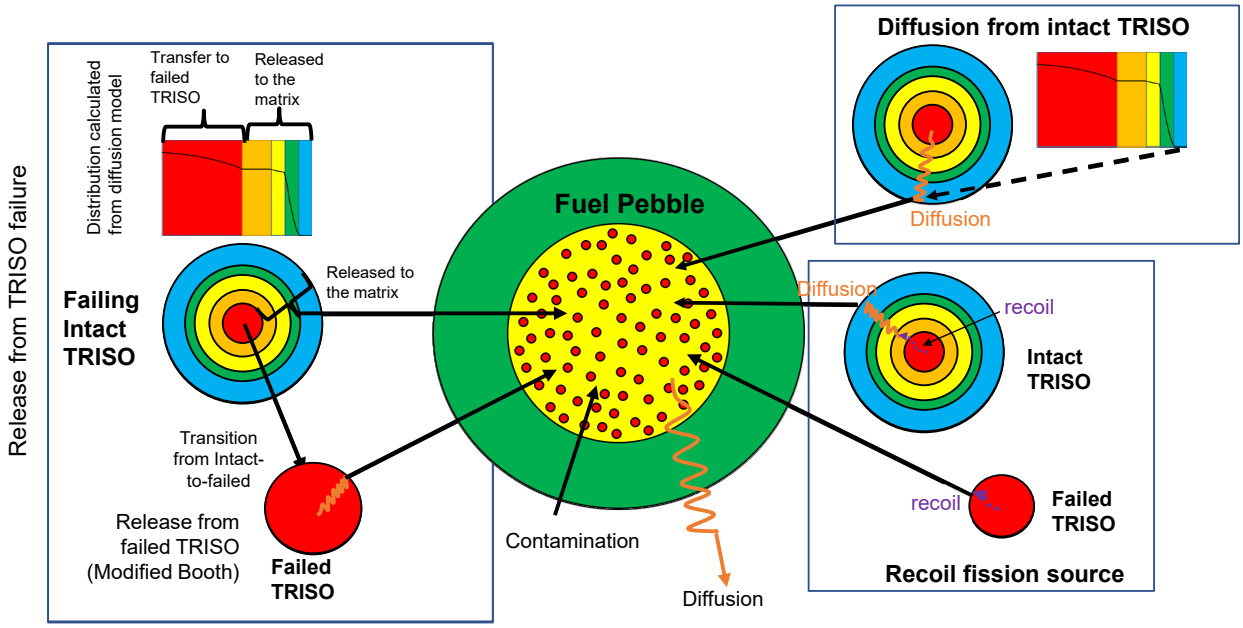

Figure 2-1 MELCOR PBMR radionuclide release models.

2.2. MELCOR HTGR Solution Methodology

A MELCOR HTGR accident simulation is performed in a single calculation and includes four stages (see Figure 2-2). The model is initialized to the normal plant operating conditions in Stage 0. Any discrepancies in the user-specified initial conditions are updated as the model's boundary conditions drive the temperature, pressure, and flow conditions to the desired normal operating conditions. Special steady state acceleration models allow the long-term convergence of the heat structure temperature distribution prior to the start of the calculation.

Stage 1 of the steady state calculates the long-term radionuclide transport and releases during normal operating conditions. For the PBMR-400 demonstration problem, the accident is assumed to occur after 900 days of operation. The accelerated diffusion model predicts the steady state distribution of the various radionuclides through the TRISO finite volume computational meshes for the intact TRISO, the failed TRISO, and the pebbles for each COR cell in the reactor core. At the completion of the long-term steady state diffusion phase of the accident, the radionuclide release and graphite dust generation from 900 days of operation exists in the primary system, including the long-term deposition onto the reactor vessel and primary system piping and walls. The steady state diffusion

model also generates the long-term (900 day) distribution of the non-released radionuclides between the fuel kernel, the various TRISO layers, and the pebble matrix.

Stage 2 is the non-accelerated transient diffusion phase. The transient diffusion phase of the simulation shifts the physics models for the radionuclide transport to transient calculations. The transient calculations end all time accelerations and activate the TRISO failure modeling in anticipation of the fourth phase.

Finally, Stage 3 is driven by imposed boundary conditions for the accident simulation (e.g., a break in the recirculation piping). The transient radionuclide diffusion models and TRISO failure models respond to the new conditions and calculate the radionuclide releases in the final phase of calculation.

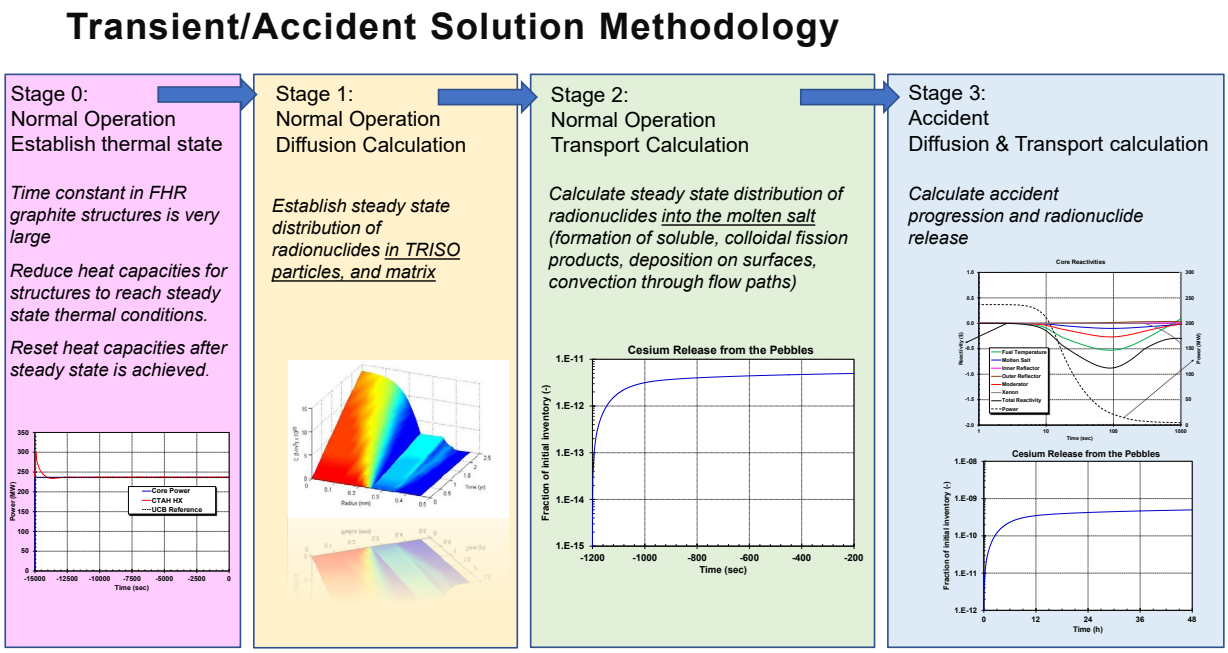

Figure 2-2 MELCOR HTGR solution methodology.

3. MODEL DESCRIPTION

The development of the MELCOR PBMR-400 input model was started at TAMU prior to 2010 [4]. The model was developed for thermal-hydraulic comparisons to benchmark data from an OECD/NEA PBMR-400 code benchmark activity [7]. At the time of the TAMU effort, a prototypic HTGR called the NGNP was being planned. At the same time, SNL was enhancing MELCOR with HTGR modeling capabilities for the NRC in anticipation of licensing activities. The TAMU project developed the first plant model of a HTGR to exercise the new MELCOR HTGR models.

The scope of the TAMU analysis did not include all the components required for an MST evaluation. Furthermore, significant MELCOR HTGR code development work has been ongoing since 2010 to enhance capabilities for pebble bed heat transfer, radionuclide release from TRISO pebbles, and an integration of the long-term radionuclide generation and diffusivity models with the transient calculation models. Consequently, the initial activities for this project involved reconciling the TAMU input model with the updated MELCOR models and input requirements. The updated input requirements and phenomenological models are documented in the latest versions of the MELCOR user guide and reference manual [8]. The remaining tasks included incorporation of the SCALE radionuclide inventory, decay heat tables, and power profiles from ORNL, incorporation of TRISO fission product release models, a point kinetics model, a confinement building, the passive reactor cavity cooling system, and the radionuclide tracking algorithms.

The PBMR-400 model nodalization is described in Section 3.1. It includes a description of the reactor vessel, the primary system, the secondary system, the passive reactor cavity cooling system (RCCS), and the confinement. Section 3.2 describes the fission product inventory and decay heat input provided from ORNL. The fission product release data are described in Section 3.3, which includes the fission product diffusivity through the TRISO fuel particles and the graphite pebbles. The point kinetics model is described in Section 3.4, and the steady state initialization is described in Section 3.5.

3.1. PBMR-400 Model Nodalization

The full-plant PBMR-400 model nodalization and key modeling features for the reactor vessel, the primary and secondary systems, and the confinement and RCCS are described in Sections 3.1.1 through 3.1.3, respectively.

3.1.1. Reactor Vessel Nodalization

The scope of the TAMU effort included the reactor vessel with specified inlet and outlet boundary conditions from the OECD code benchmarking project [6]. The PBMR-400 reactor vessel is shown in Figure 3-1. The vessel is very tall and includes an 11 m high annular core of the fuel pebbles that is surrounded by graph reflectors on the outside, the top, the bottom, and on the inside. The massive reflectors surrounding the annular fuel region and the low ~5MW/m^3 power density are key components of the passive heat dissipation design [9]. The reflectors absorb heat away from the fuel to mitigate the peak temperature response to loss-of-forced cooling events, thereby eliminating the requirements for an active core heat removal system. The design includes recirculation and replacement of the fuel pebbles to permit long-term and uniform power operation.

Reference [9] describes the stacked vertical columns of graphite reflector blocks that are supported by the core barrel assembly. The helium gas enters the bottom of the reactor where it flows through riser in the side reflector to the inlet plenum at the top of the pebble bed. The gas then flows down

through the pebble bed where it is heated. The gas exits from the lower plenum to an outlet pipe. Some of the key reported parameters for the reactor are summarized in Table 3-1.

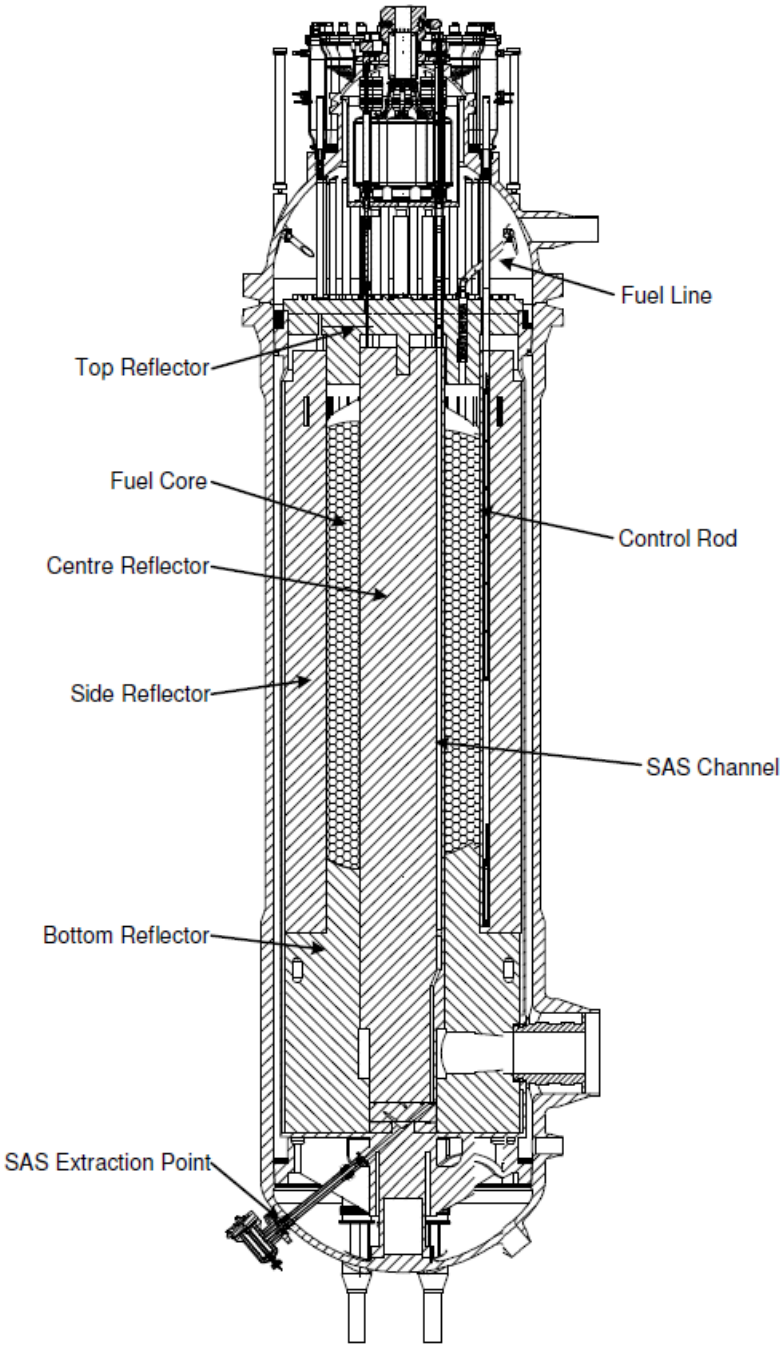

Figure 3-1 PBMR-400 reactor vessel [9].

Table 3-1 Key parameters for the PBMR-400 [9].

Parameter	Value
Reactor thermal power	400 MW
Coolant	Helium
Reactor inlet temperature	500ºC
Reactor outlet temperature	900ºC
Operating pressure	9 MPa
Pebble bed inner diameter	2.0 m
Pebble bed outer diameter	3.7 m
Pebble bed height	11.0 m
Vessel flowrate	192 kg/s
Pebble bed volume	~84 m^3
Number of pebbles	~452,000
Target burn-up	92,000 MWd/tU

The modeling of the PBMR-400 reactor vessel in MELCOR utilizes building block inputs from multiple packages. The building block approach to the input gives flexibility to model many reactor designs with varying levels of resolution. A key set of input comes from the COR Package, which includes the fuel pebbles, the reflectors, and the radionuclide release model. The PBMR-4000 COR nodalization is shown in Figure 3-2, which is faithful to the aspect ratio of the reactor and the relative spacing of the 29 axial levels and 8 radial rings. The COR nodalization uses cylindrical coordinates which includes (a) the active core region with the pebbles (i.e., shaded region within axials levels 6-27 and rings 2-6), (b) the center, top, bottom, and outer radial reflectors surrounding the pebble bed, (c) the inlet plenum in axial level 28, (d) the outlet plenum in axial levels 2-5, and (e) the inlet riser to the inlet plenum in ring 8. The COR package includes the heat transfer and physics routines for the materials in the core, any material relocation and the eutectic interactions, the supporting structure degradation, the lower reactor head heatup and failure, and all the routines for the radionuclide release from the TRISO fuel pebbles (i.e., discussed in Section 3.2).

In the demonstration calculation, there is no relocation of materials. Although the graphite structures did not collapse, there was some degradation due to oxidization from an ingress of air. Consequently, the TRISO fuel pebbles remained stationary in the COR region. The active COR cells are equally spaced (0.5 m high and 0.7 m ring-to-ring spacing) but are not equal in volume due to the cylindrical geometry. Ring 1 contains the inner reflector and has a 1 m radius. The outer reflector and inlet riser in rings 7 and 8 have outer radii of 2.436 m and 2.606 m, respectively. The outer radius of the COR nodalization connects to a small gap between the outer graphite reflector and the stainless steel core barrel structure. The reactor cross-section, shown in Figure 3-3, illustrates many of these components including the inlet riser, the core barrel, and the fuel region.

The fueled COR cells contain the graphite pebble with the TRISO fuel. The pebbles are modeled with the fuel (FU) component for the UO_2 kernel, graphite for the non-fueled portion of the pebble

as an additional FU component, and matrix (MX) for the pebble outer shell. As discussed in Reference [4], the mass of UO_2 in the cell's fuel component is determined by calculating the number of pebbles in the cell (equal to the total cell volume times the packing fraction 0.61, divided by the volume of one pebble) and multiplying by the mass of UO_2 per pebble (0.0102 kg). The additional FUEL graphite mass is calculated by determining the number of pebbles in the cell and multiplying by the mass of graphite in the fueled region of one pebble, which is equal to the volume of the fueled region of a pebble minus the volume of UO_2 times the density of graphite. Finally, the MATRIX mass is calculated by multiplying the number of pebbles in the cell by the mass of graphite in the shell around a pebble, which is equal to the volume of the shell times the density of graphite.

The surrounding graphite reflectors are modeled using the COR reflector (RF) component. The mass of the reflector is equal to the volume of the COR cell minus the volume of the flow channels and plenums. Reference [4] notes there is a small bypass flow that goes through the center reflector, which was neglected (i.e., consistent with a recommendation for the PBMR-400 benchmark [6]). Per MELCOR input requirements, the graphite reflector in axial level 5 was designated as a supporting structure (SS) to support the pebble bed fuel. The graphite in axial level 29 was also defined as SS because the RF component cannot be supported by the open inlet plenum. The SS component was used at axial level 1 to represent the stainless steel support structure at the bottom of the lower reflector. Ring 8 included the flow channels for the inlet gas flow to the upper plenum and the surrounding graphite (see Figure 3-3).

The corresponding MELCOR nodalization for the control volumes (CVs) in the CVH package and the flow paths (FP) in the flow paths in the flow path (FL) package are shown in Figure 3-4. Unlike Figure 3-2, the aspect ratio of the reactor vessel is stretched to improve the identification of the CVH and FL components. MELCOR requires every COR cell to have a corresponding control volume.[1] The COR nodalization axial and radial boundaries from Figure 3-2 are shown on Figure 3-4 using dashed blue lines. The CVs are shown separated from one another to provide room to show the interconnecting flow paths.

The CVs in Ring 1 (i.e., CV-110 though CV-115) are small (negligible) fluid volumes without any interconnecting flow paths. Similarly, the CVs in Ring 6 (CV-171 and CV-182) and in axial level 29 (CV-115 and CV-126 through CV-186) are prescribed as small CVs to satisfy input requirements.

As shown in the figure, multiple core cells can be connected to a single control volume. This is done for computational efficiency and is typical of a MELCOR model. MELCOR includes a model in the COR package when multiple COR cells connect to a single CV to resolve the local COR cell temperature distribution and associated structure to fluid heat transfer.

The remaining CVs and FPs in Figure 3-4 represent the primary flow paths for the high-temperature helium. The fluid enters through FL-640 to the inlet risers in CV-181. The fluid rises through the riser channels to the inlet plenum in CV-170. The flow is distributed in the inlet plenum to flow

[1] This requirement has its origins for LWR applications where there are usually no large solid reflectors around the core (e.g., the NuScale small modular reactor and the Russian RBMK reactors would be examples of exceptions). If the materials in the COR cell relocate, then there is an open void. Consequently, the CV expands to fill the void. There was no relocation of core materials in the demonstration calculation. Consequently, the CV requirement was satisfied by prescribing a small volume CV.

downward into the five COR rings in the PBMR-400 MELCOR nodalization. The gaps between the outer radial graphite reflector and the core barrel and the core barrel and the vessel wall are represented by CV-401 and CV-51, respectively. These gaps are stagnant without any flow connections. The heat that is transferred in the outward radial direction from the pebble bed to outside of the vessel must pass across these gaps.

The radial and axial heat transfer within the pebble bed is modeled using a modified version of the Zehner-Schlunder-Bauer unit cell approach. The main component of the heat transfer at high temperature is radiation but conduction through the pebbles and the fluid and direct conduction through the pebbles at their contact points is included. The model was recently updated to extend the radial heat transfer from the pebble bed to the reflector (RF) and supporting structure (SS) components around the pebble bed. The implementation and model assumptions are discussed in the MELCOR reference manual[8]. The COR package axial and radial radiation model is disabled in lieu of this modeling approach.

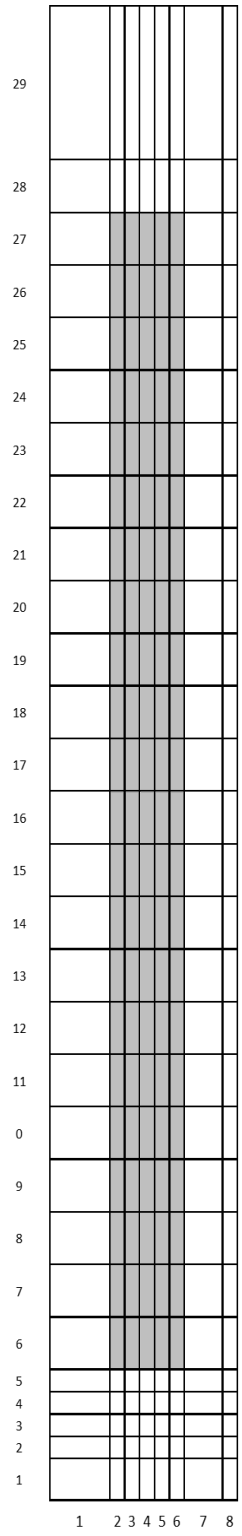

Figure 3-2 PBMR-400 COR nodalization.

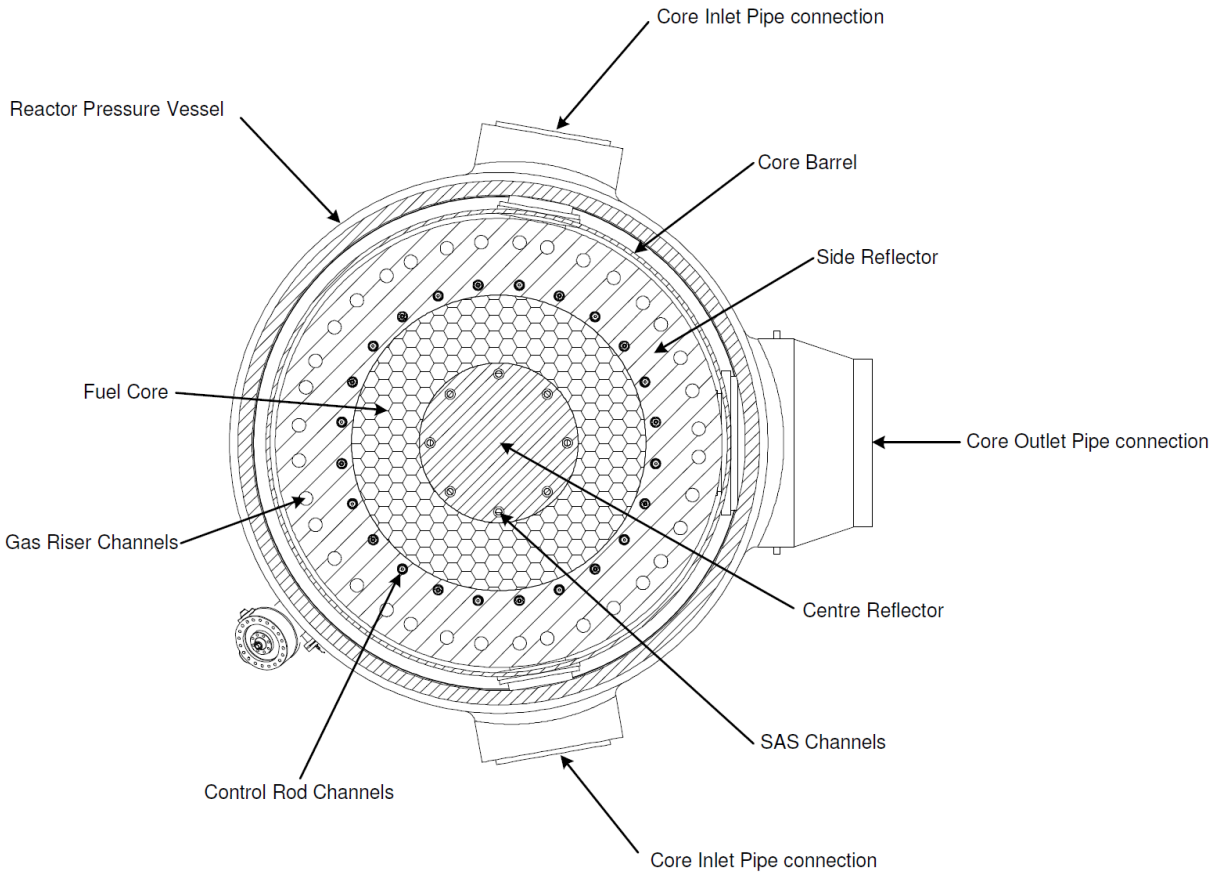

Figure 3-3 PBMR-400 radial cross-section [9].

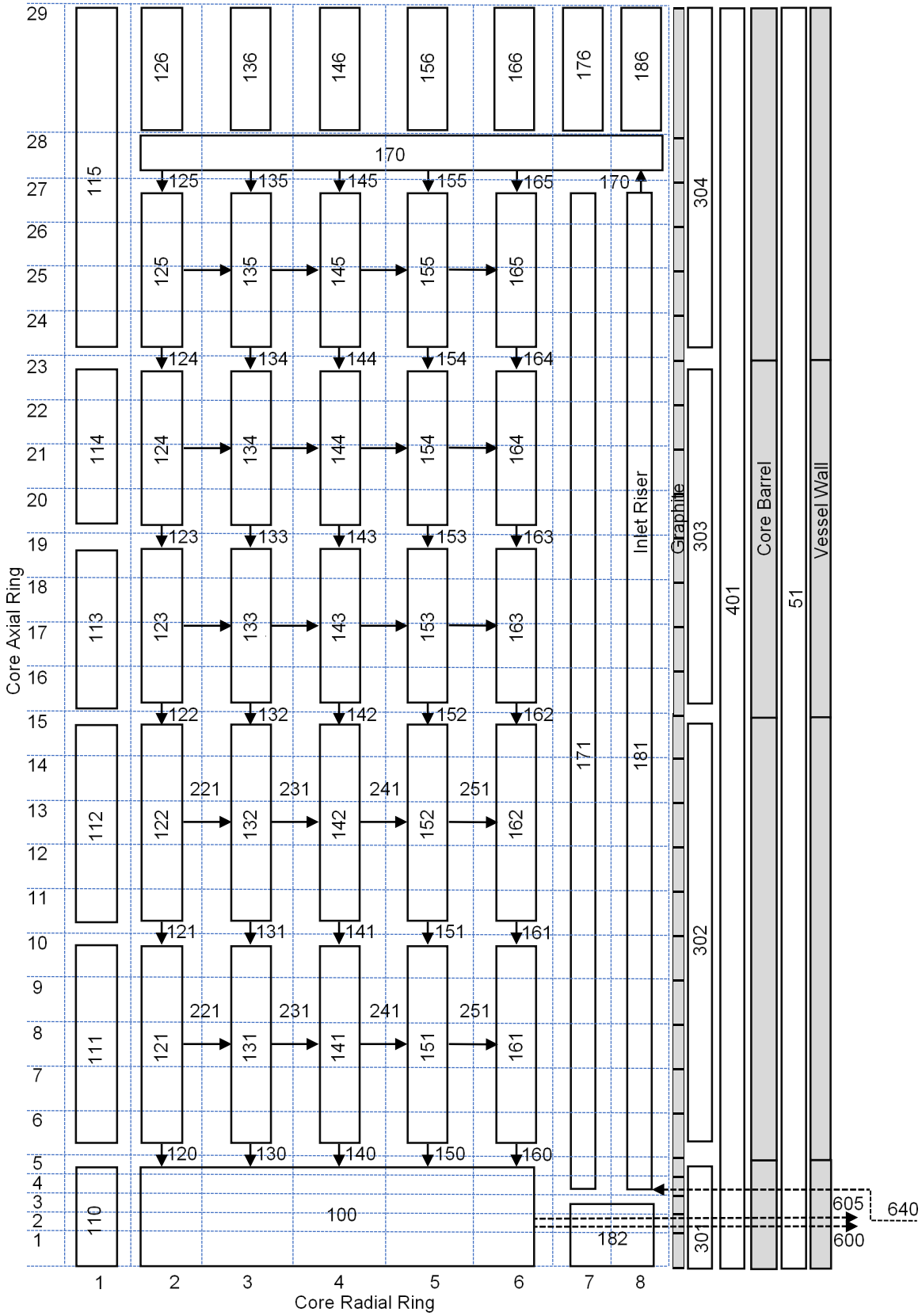

Figure 3-4 PBMR-400 vessel CVH and FL nodalization.

3.1.2. Primary and Secondary System Nodalization

The PBMR-400 recirculation loop was not part of the PBMR-400 model documented in Reference [4] nor the OECD benchmark [6]. Furthermore, the construction of the PBMR-400 demonstration plant using a recuperative Brayton cycle recirculation loop was abandoned. Newer pebble bed reactor designs, such as the DOE NGNP design, featured a conventional steam generator or other gas-to-gas intermediate heat exchangers to supply hot gas for process heat (e.g., see Appendix B of Reference [10]). Due to the lack of reference information for the PBMR-440 recirculation loop, a simplified nodalization was used (see Figure 3-5). The primary heat exchanger provides the appropriate boundary condition for the steady state but has a negligible role thereafter in the scenarios evaluated in the demo calculations.

The PBMR-400 recirculation loop includes the hot leg leaving the bottom of the vessel, the heat exchanger, the cold leg return to the inlet riser at the bottom of the vessel, and the helium circulator. During the steady state, the helium flows from the vessel to the heat exchanger, and then back to the vessel. The hot leg piping is assumed to be completely severed at the start of the DLOFC transient, which quickly depressurizes the recirculation loop and the reactor vessel. This is accomplished by closing FL-610 and FL-615 and opening FL-625, FL-626, and FL-627 (see Figure 3-6). The flow in the recirculation loop somewhat stagnates after system depressurizes. However, a small counter-current natural circulation flow is established between the vessel outlet plenum and the broken hot leg piping. The hot gas in the vessel lower plenum flows out the top of the broken hot leg piping (CV-605), which is replaced by cooler gas from the confinement through the bottom of the broken hot leg (CV-600). Although FL-625 shows an arrow pointing outward from CV-600 (i.e., MELCOR requires a specified from/to orientation), the natural circulation flow on this pathway is negative, or into the vessel.

Finally, the drag between the adjacent flow paths in CV-605 and CV-600 is modeled using MELCOR's counter-current flow limiting model. The drag coefficient between the inlet and outlet gas streams was specified in the same manner as a pressurized water reactor hot leg natural circulation flow during severe accident conditions [11]. The counter-current stratified flow model limits the air exchange based on a Froude Number correlation for drag between horizontally stratified flows.

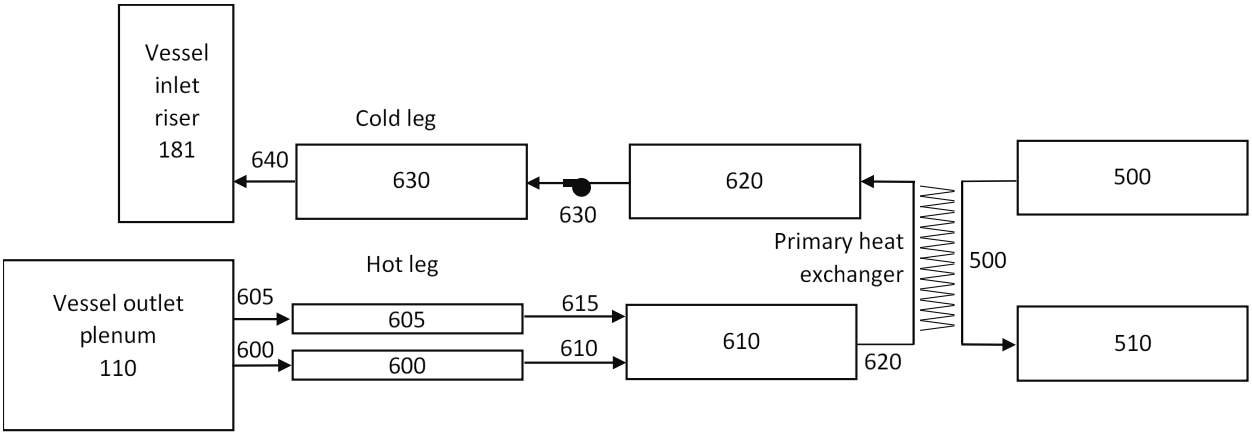

Figure 3-5 PBMR-400 primary and secondary CVH and FL nodalization during the steady state.

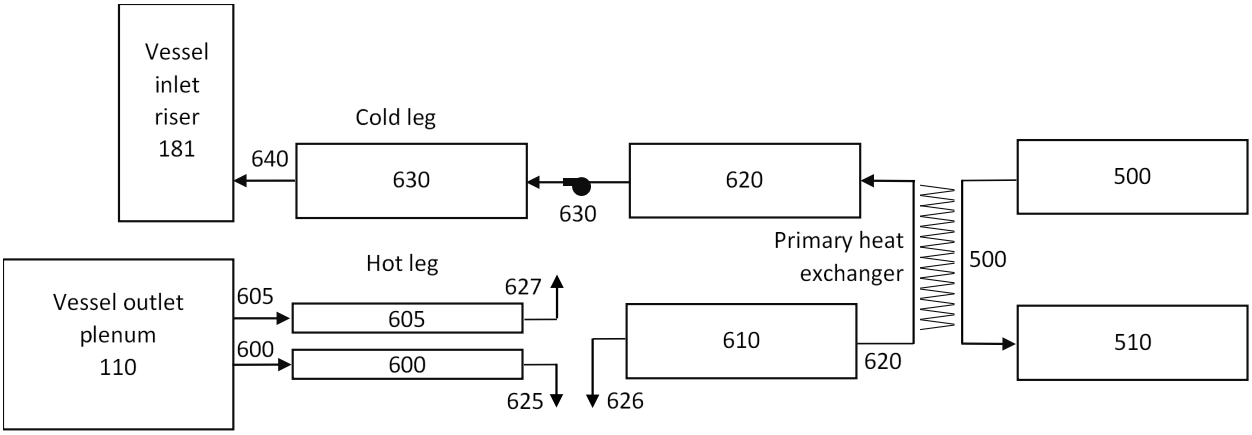

Figure 3-6 PBMR-400 primary and secondary CVH and FL nodalization during the DLOFC scenario after the hot leg pipe break.

3.1.3. Confinement and Reactor Cavity Cooling System Nodalization

Similar to the recirculation system, the PBMR-400 benchmark did not include a confinement building. For this demonstration calculation, a confinement building was developed based on the DOE NGNP schematic as illustrated in Reference [10]. The room volumes and dimensions were estimated by scaling off drawings (i.e., see NGPN schematic and the PBMR-400 nodalization in Figure 3-7. The reactor and steam generator are located in below-grade compartments. The above-grade compartment contains the refueling machine. The NGNP shown in in Figure 3-7 has a water-based RCCS whereas the PBMR-400 has an air-flow RCCS (e.g., see Figure 3-8).

There are two CVs around the vessel, CV-50 and CV-51. CV-50 is required by MELCOR to represent the region around the outside of the reactor lower head. CV-51 is the gap between the reactor vessel and the RCCS heat transfer panels. There is convective and radiative exchange across the air gap from the vessel to the RCCS heat transfer panels. The RCCS consists of an inlet, downcomer, and four CVs for the riser section adjacent to the heat transfer panels. The heated air rises upward and exits the building. Areva provides illustrations of many RCCS concepts in Reference [12], including water systems. The airflow RCCS in the PBMR-400 is one of the examples, as shown in Figure 3-8.

The building leakage size is specified as 3.3 in^2, based on scaling to the reactor building surrounding a boiling water reactor (i.e., 100% leakage per day at a design pressure of 0.25 psi). Due to the energetic blowdown of the primary system in the DLOFC, the building is assumed to include an above-grade passive flapper that releases the pressure from the confinement during the blowdown. The schematic in Figure 3-7 may indicate these compartments are isolated from the upper confinement. In the current calculations, the compartments containing the reactor and steam generator are assumed to have open flow connectivity with the upper containment. The DLOFC pipe break is assumed to occur in the piping between the reactor and the steam generator compartments. The flapper closes after the blowdown and the building reverts to atmospheric pressure.

When there is an external wind, one flow path is assigned to the upwind side of the building and the other is on the downwind side. The guidance for modeling building wind effects is described in Reference [13]. External wind effects are included in DOE facility safety analysis where there also

are not strong driving forces. The wind increases building infiltration and exfiltration rates. Both an upwind infiltration location and a downwind location were included in the model. The wind effects are modeled as an additional Bernoulli pressure term in the flow path pressure solution,

$$dP_{Wind} = \frac{1}{2}\rho C_p v^2$$

where,

dP_{Wind}	Bernoulli wind pressure term, (Pa)
ρ	Fluid density, (kg/m^3)
C_p	Building coefficient, (-)
v	Wind velocity, (m/s)

The values for building coefficients are typically obtained using computational fluid dynamics evaluations. When wind effects are modeled in the demonstration calculations, generic values were obtained from the American Society of Heating, Refrigerating and Air-Conditioning Engineers (ASHRAE) handbook (see Table 3-2 [14]).

Table 3-2. Typical building coefficients [14].

Wind Direction	Value
Upwind	0.7
Downwind	-0.4
Side and top of the building	-0.35

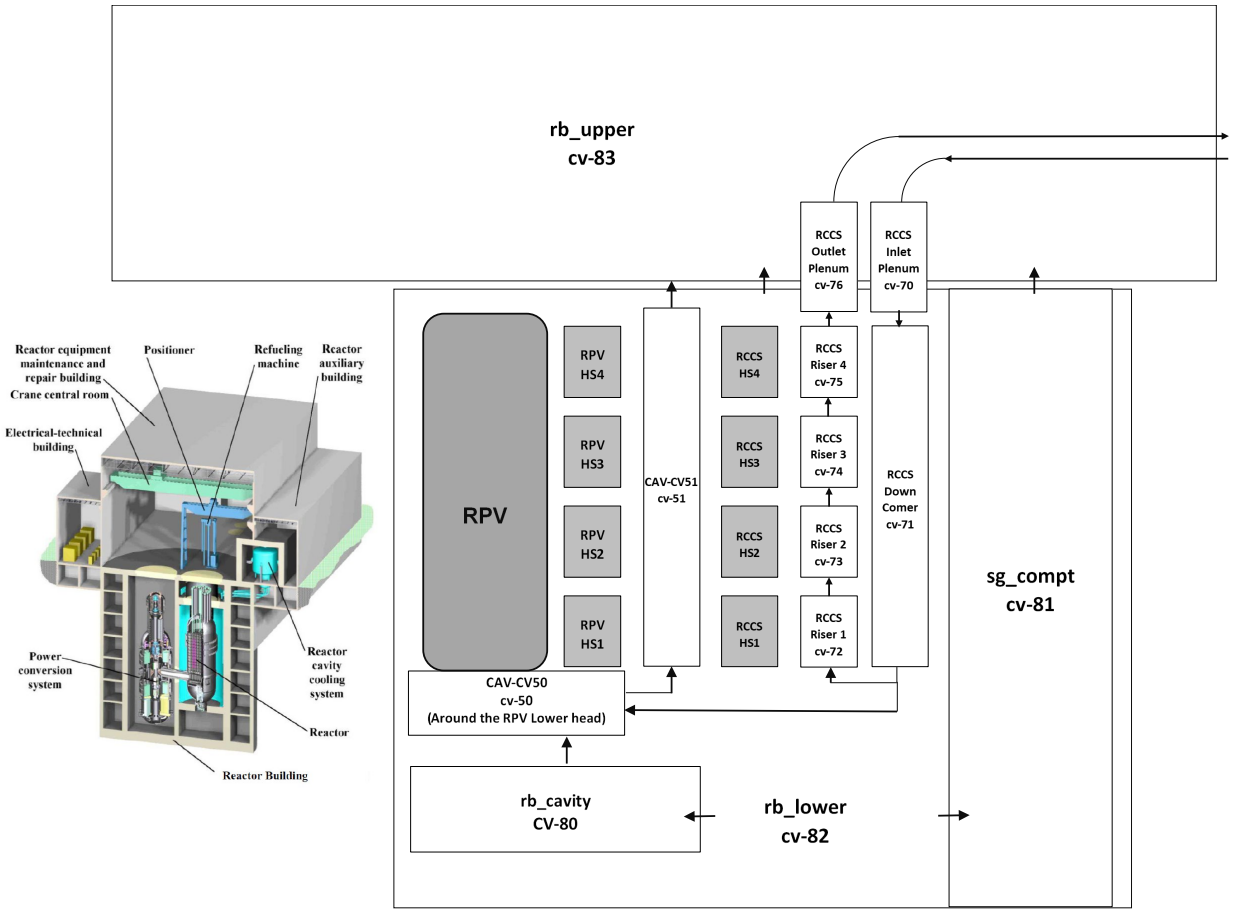

Figure 3-7 PBMR-400 confinement CVH and FL nodalization with NGNP schematic [10].

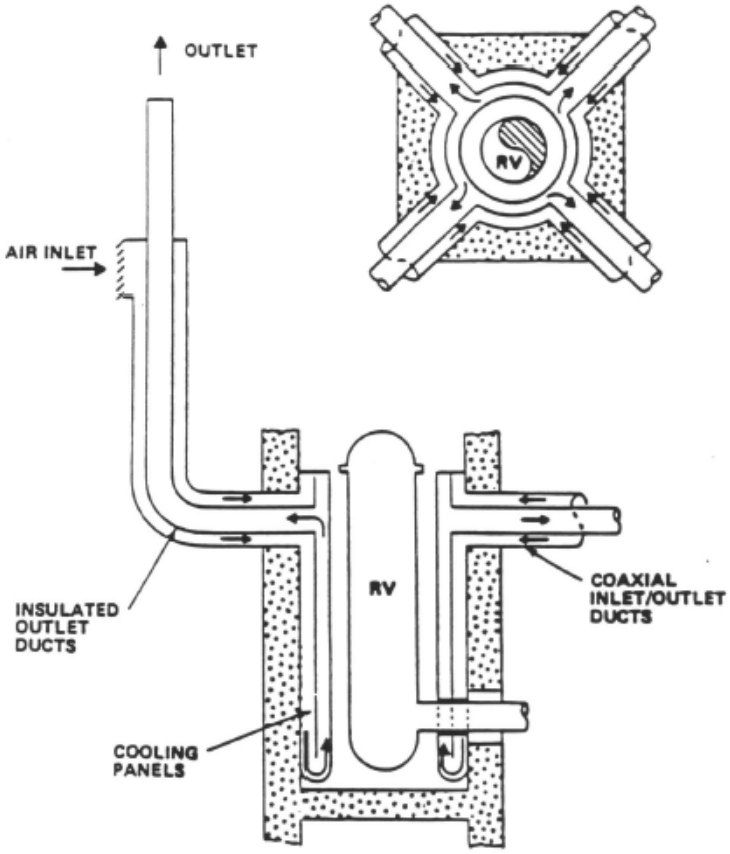

Figure 3-8 Example of an airflow RCCS [12].

3.2. Radionuclide Inventory and Decay Heat Input

The radionuclide inventory and decay heat inputs were calculated using SCALE by Oak Ridge National Laboratory (ORNL). The radionuclides from the SCALE calculation are grouped and assigned to one of the twelve MELCOR radionuclide classes (see Table 3-3). ORNL provided multiple burn-up results that could be used to approximate the continuous refueling of a PBMR-400. As a simplification, the maximum 90 GWd/MTU burn-up inventory and decay heat was used for all pebbles throughout the core. The data provided from SCALE includes separate decay heat curves for each radionuclide class in Table 3-3. The radionuclide class inventories are shown in Table 3-4 and the overall decay is shown in Figure 3-9.

Table 3-3 MELCOR radionuclide classes

Class	Class Name	Chemical Group	Representative	Member Elements
1	XE	Noble Gas	Xe	He, Ne, Ar, Kr, Xe, Rn, H, N
2	CS	Alkali Metals	Cs	Li, Na, K, Rb, Cs, Fr, Cu
3	BA	Alkaline Earths	Ba	Be, Mg, Ca, Sr, Ba, Ra, Es, Fm
4	I2	Halogens	I_2	F, Cl, Br, I, At
5	TE	Chalcogens	Te	O, S, Se, Te, Po
6	RU	Platinoids	Ru	Ru, Rh, Pd, Re, Os, Ir, Pt, Au, Ni
7	MO	Early Transition Elements	Mo	V, Cr, Fe, Co, Mn, Nb, Mo, Tc, Ta, W
8	CE	Tetravalent	Ce	Ti, Zr, Hf, Ce, Th, Pa, Np, Pu, C
9	LA	Trivalents	La	Al, Sc, Y, La, Ac, Pr, Nd, Pm, Sm, Eu, Gd, Tb, Dy, Ho, Er, Tm, Yb, Lu, Am, Cm, Bk, Cf
10	UO_2	Uranium	UO_2	U
11	CD	More Volatile Main Group	Cd	Cd, Hg, Zn, As, Sb, Pb, Tl, Bi
12	AG	Less Volatile Main Group	Ag	Ga, Ge, In, Sn, Ag

Table 3-4 PBMR-400 radionuclide class masses.

MELCOR RN class	MELCOR Class Mass (kg)
Noble Gases (Xe)	65.2
Alkali Metals (Cs)	34.4
Alkaline Earths (Ba)	27.9
Halogens (I)	2.13
Chalcogens (Te)	5.73
Platinoids (Ru)	37.3
Early Transition Elements (Mo)	46.6
Tetravalent (Ce)	122.8
Trivalents (La)	86.5
Uranium (U)	3633.7
More Volatile Main Group (Cd)	0.68
Less Volatile Main Group (Ag)	1.00

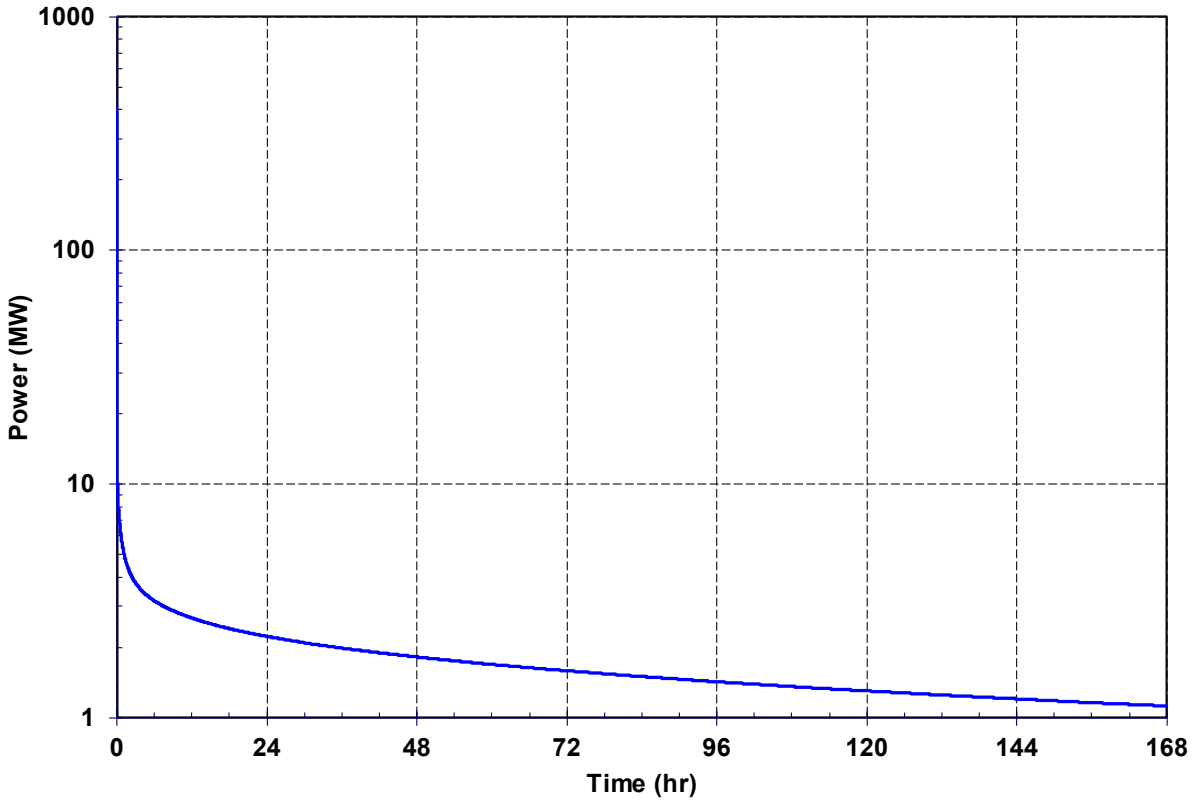

Figure 3-9 PBMR-400 decay heat curve.

3.3. Fission Production Release

The MELCOR fuel diffusivity model calculates the release of fission products from the TRISO-fuel pebbles in the core. Figure 2-1 shows the key processes included in the model. The model calculates the distribution of the fission products generated and released during normal power operation and during an accident. The steady state distribution of fission products generated in the fuel kernels (i.e., set to the values provided by SCALE) includes the amount recoiled and diffused to the buffer layer, the amount diffused through the dense coating layers, the amount released from the kernels of particles with failed coating layers, and the amount which diffuses through the pebble graphite matrix (e.g., see Figure 2-1 for various types of radionuclide release). Following release from the pebbles, the MELCOR radionuclide vapor and aerosol behavior model calculates the transport and deposition of fission products in the reactor system and reactor building.

The MELCOR fuel diffusivity release model includes important phenomena for fission product behavior in HTGRs [15]. The model considers two types of TRISO particles: those with intact coating layers and those with failed coating layers (e.g., see the intact TRISO model in Figure 3-10). A small fraction of the fuel particles is also modeled as initially failed due to manufacturing defects, which was specified to be 10^{-5}. The fraction of failed particles during accidents or transients can be specified using MELCOR's temperature-based, empirical correlation. However, there are provisions for user-specified model. The demo calculation used the default temperature correlation, which was developed from German post-irradiation failure tests.

For intact TRISO, the gaseous fission products released from the fuel kernel are assumed to accumulate in the buffer; for failed particles, fission products are assumed to go directly to the graphite matrix. The condensable (metallic) and non-condensable (gaseous) fission product releases are calculated using diffusion-based release models. The diffusion calculation determines the distribution of the fission product inventory between the kernel and the various TRISO layers, and the amount released from failed particles. There are also contributions to fission products from uranium contamination in the graphite matrix, which is specified to be a very small fraction of the total fuel inventory (i.e., 10^{-6}).

A key input for the MELCOR diffusivity model is the radionuclide-specific diffusivity data. The International Atomic Energy Agency (IAEA) published a comprehensive review of fuel performance and fission product behavior in gas-cooled reactors (i.e., Reference [16]). The objectives of the IAEA international cooperative research program were to review and document the status of the experimental data base and of the predictive methods for gas-cooled reactor fuel performance and fission product behavior; and to verify and validate methodologies for the prediction of fuel performance and fission product transport. The participants included institutions from Germany, Japan, the United States, Russia, China, France, and the United Kingdom. There are limited diffusivity data for radionuclide transport through TRISO fuel. The key measured radionuclides are cesium, krypton, strontium, and silver. Appendix A of the IAEA report provided a comprehensive set of diffusivity data. Table 3-5 summarizes the data. Although there were no reported data for the buffer region between the kernel and the inner pyrolytic carbon layer, a recommended value was provided. It was also suggested the values for krypton would be appropriate for iodine gas.

The MELCOR PBMR-400 fuel diffusivity release model tracked 5 elements (i.e., cesium, krypton, strontium, silver, and iodine). It was assumed that iodine transported the same as krypton. The remaining radionuclide classes were modeled using MELCOR's CORSOR-Booth radionuclide release scaling factors. The CORSOR-Booth model for radionuclide release was validated to experimental results from the light-water reactor VERCORS experiments and benchmarked to Phebus data [17]. Although there are inadequate data to adjust the release coefficients for the TRISO fuel pebbles, LWR scale factors were used as a surrogate to estimate additional radionuclide contributors to the accident source term. The LWR scaling factors are shown in Table 3-6. The LWR radionuclide class scaling factors are applied to chemically similar elements in the various radionuclide classes shown in Table 3-7. The LWR scaled release factors in Table 3-6 and radionuclide class definitions in Table 3-7 are presented to illustrate code capabilities rather than an endorsement of their appropriateness for TRISO-based systems. As more TRISO diffusivity data becomes available, then the new elements can be added to the fuel diffusivity release model and the elements in the associated radionuclide classes can be appropriately adjusted.

A TRISO failure model is built into the MELCOR code (see Figure 3-11) but can be replaced using user-input [8]. MELCOR's default failure curve was developed from a statistical analysis of the post-irradiation testing of primarily German AVR TRISO fuel up to 1800 °C. The curve was developed using UO_2 TRISO fuel, which is consistent with the PBMR-400 design.

The fission products released during normal operation can accumulate on the graphite dust that is generated and subsequently distributed system and deposits on surfaces in the primary system. The graphite dust is generated primarily due to abrasion between pebbles during the high-velocity circulation of the helium gas through the core. The demo calculation assumes approximately 24 kg of dust is generated each year based on scaled observations from the German AVR HTGR [18]. In

the DLOFC accident scenario, some of the radioactive dust is predicted to be resuspended from the surfaces due to the high velocities during the primary system depressurization.

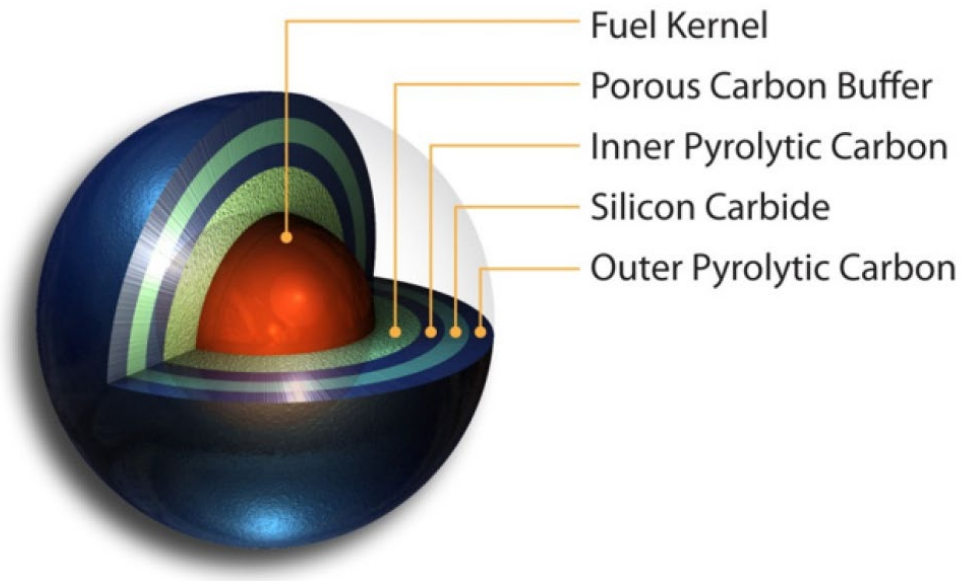

Figure 3-10 MELCOR intact TRISO model [19].

Table 3-5 Diffusivities used in the PBMR-400 model [16]

Layer	FP Species							
	Kr		Cs		Sr		Ag	
	$D_{o,i}$ (m^2/s)	Q_i (J/mole)	$D_{o,i}$ (m^2/s)	Q_i (J/mole)	$D_{o,i}$ (m^2/s)	Q_i (J/mole)	$D_{o,i}$ (m^2/s)	Q_i (J/mole)
Fuel kernel	1.3×10^{-12}	126000.0	5.6×10^{-8}	209000.0	2.2×10^{-3}	488000.0	6.7×10^{-9}	165000.0
Buffer	1.0×10^{-8}	0.0	1.0×10^{-8}	0.0	1.0×10^{-8}	0.0	1.0×10^{-8}	0.0
PyC	2.9×10^{-8}	291000.0	6.3×10^{-8}	222000.0	2.3×10^{-6}	197000.0	5.3×10^{-9}	154000.0
SiC	$3.7\times10^{+1}$	657000.0	7.2×10^{-14}	125000.0	1.2×10^{-9}	205000.0	3.6×10^{-9}	215000.0
Matrix Carbon	6.0×10^{-6}	0.0	3.6×10^{-4}	189000.0	1.0×10^{-2}	303000.0	1.6	258000.0
Str. Carbon	6.0×10^{-6}	0.0	1.7×10^{-6}	149000.0	1.7×10^{-2}	268000.0	1.6	258000.0

The coefficients above are used to calculate the local diffusivity using an Arrhenius type equation as a function of temperature.

$$D = \sum_i D_{o,i} \exp\left(\frac{Q_i}{RT}\right)$$

where,

i is the index when multiple coefficients are specified (i=1 in demo)
$D_{o,i}$ is the pre-exponential factor [m^2/s]
Q_i is the activation energy [J/mol]
T is the local temperature [K]
R is the universal gas constant [J/mol-K]

Table 3-6 CORSOR-Booth radionuclide release scaling factors [8].

Class	Scaling Factor
Te	0.64
Ru	2.5e-3
Mo	6.25e-2
Ce	4.0e-8
La	4.0e-8
Cd	0.25

Table 3-7 MELCOR radionuclide classes [8].

Class	Class Name	Chemical Group	Representative Element	Member Elements
1	XE	Noble Gas	Xe	He, Ne, Ar, Kr, Xe, Rn, H, N
2	CS	Alkali Metals	Cs	Li, Na, K, Rb, Cs, Fr, Cu
3	BA	Alkaline Earths	Ba	Be, Mg, Ca, Sr, Ba, Ra, Es, Fm
4	I_2	Halogens	I_2	F, Cl, Br, I, At
5	TE	Chalcogens	Te	O, S, Se, Te, Po
6	RU	Platinoids	Ru	Ru, Rh, Pd, Re, Os, Ir, Pt, Au, Ni
7	MO	Early Transition Elements	Mo	V, Cr, Fe, Co, Mn, Nb, Mo, Tc, Ta, W
8	CE	Tetravalent	Ce	Ti, Zr, Hf, Ce, Th, Pa, Np, Pu, C
9	LA	Trivalent	La	Al, Sc, Y, La, Ac, Pr, Nd, Pm, Sm, Eu, Gd, Tb, Dy, Ho, Er, Tm, Yb, Lu, Am, Cm, Bk, Cf
10	UO_2	Uranium	UO_2	U
11	CD	More Volatile Main Group	Cd	Cd, Hg, Zn, As, Sb, Pb, Tl, Bi
12	AG	Less Volatile Main Group	Ag	Ga, Ge, In, Sn, Ag
16	CSI	Cesium iodide	CsI	CsI
17	CSM	Cesium molybdate	Cs_2MoO_4	Cs_2MoO_4

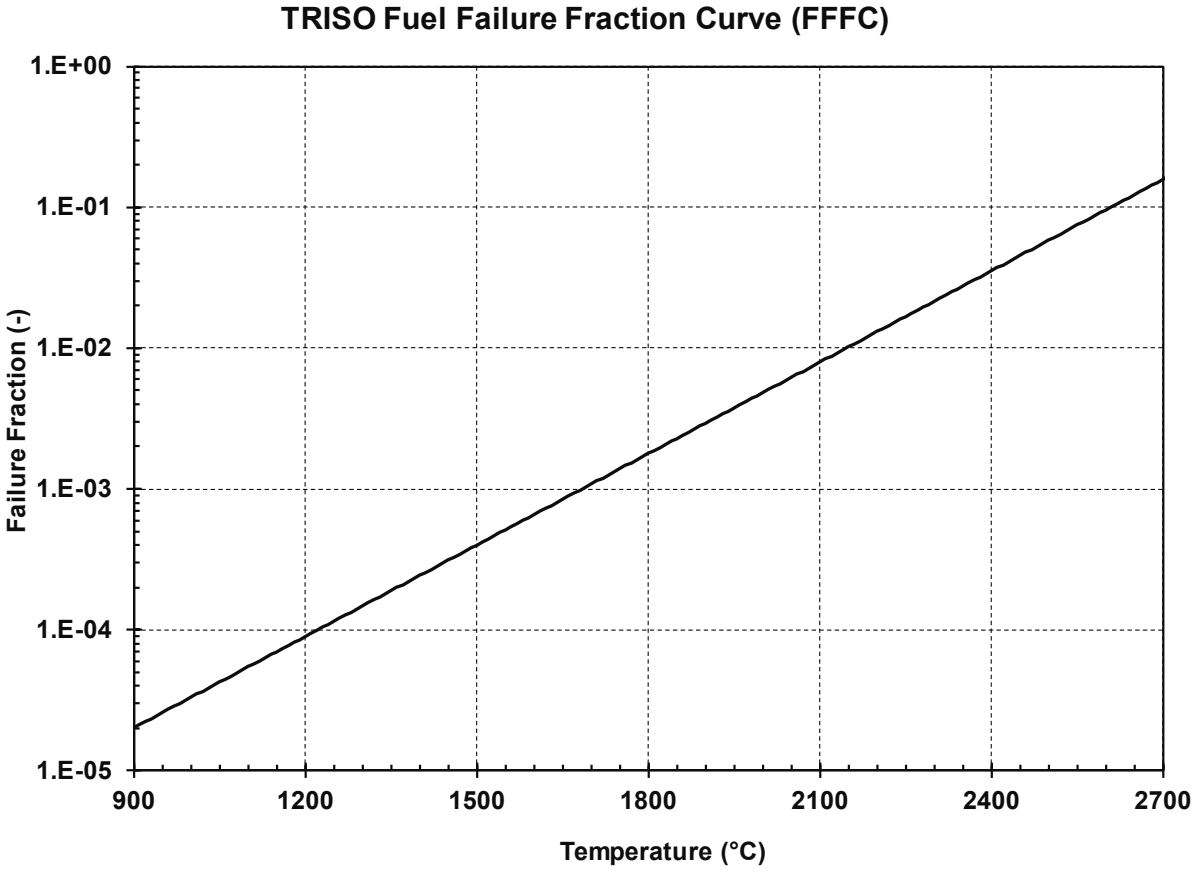

Figure 3-11 TRISO fuel failure fraction curve.

3.4. Point Kinetics Modeling

MELCOR includes a six-group point kinetics model for the dynamic simulation of the reactor power. The model was developed to support the evaluation of the DOE NGNP [20]. The PBMR-400 reactivity feedbacks were obtained from the neutronics analysis of the NGNP prismatic reactor values (see Figure 3-12). The NGNP reactivity data are used as a surrogate for the PBMR-400, which was not specifically analyzed. The NGNP feedbacks account for Doppler broadening and the fuel and graphite temperature reactivity feedback, which is described in Reference [21].

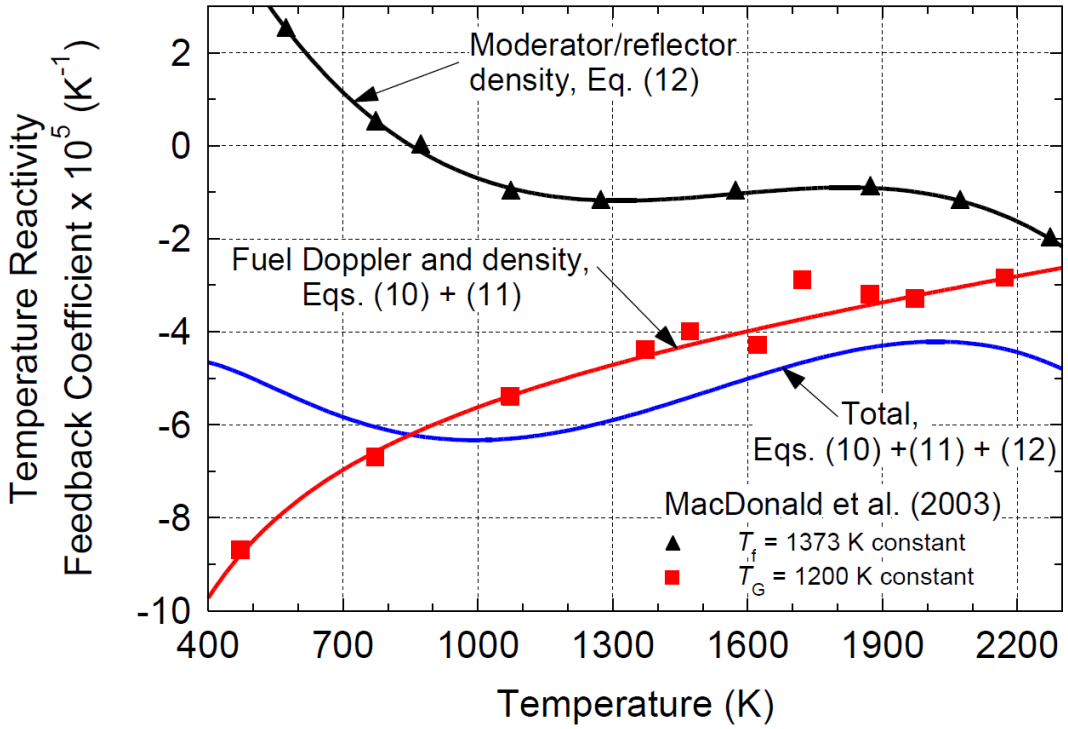

Figure 3-12 NGPN reactivity feedback curves [21].

3.5. Steady State Initialization

The PBMR-400 model was stabilized to steady state conditions. Although the results from the OECD PBMR-400 benchmark comparisons are not publicly available, the OECD benchmark specifications report include some basic thermal-hydraulic specifications [6]. Reference [4] also includes a summary of the key steady state values. Figure 3-13 through Figure 3-17 show the comparison to key steady state variables from Reference [4]. The calculated agreement with the benchmark values was good. All transient calculations used a 1350 sec steady state. However, much longer calculations were performed to establish the initial conditions for the Stage 0 portion of the calculation (see Figure 2-2). The results from the long steady state results were successively reentered into the input files over time, which permitted a shorter initialization period prior to the Stage 3 transient calculations.

The 1350 sec steady state initialization included an accelerated steady state of 900 days (Stage 1, see Figure 2-2). From -1200 sec to -200 sec, the accelerated steady state diffusion model predicted the

900-day radionuclide transport within the TRISO layers, the pebble matrix, and the any small releases to the fluid. Simultaneously, the long-term dust generation was also being calculated (i.e., 24 kg/yr, see Section 3.3).

The transition from the steady state to the transient diffusion calculation occurred at -200 sec. The 900-day release, transport, and deposition from the pebbles has completed and the model changes to normal rate of diffusion and dust generation for Stage 2. At t=0 sec, the transient calculation begins.

Prior to -100 sec, the point kinetics model was also in steady state mode and not calculating any reactivity feedbacks. The fission power is constant while the model stabilizes to steady conditions. The reactivity feedback is specified to begin at -100 sec, which allows confirmation of steady power conditions prior to the transient.

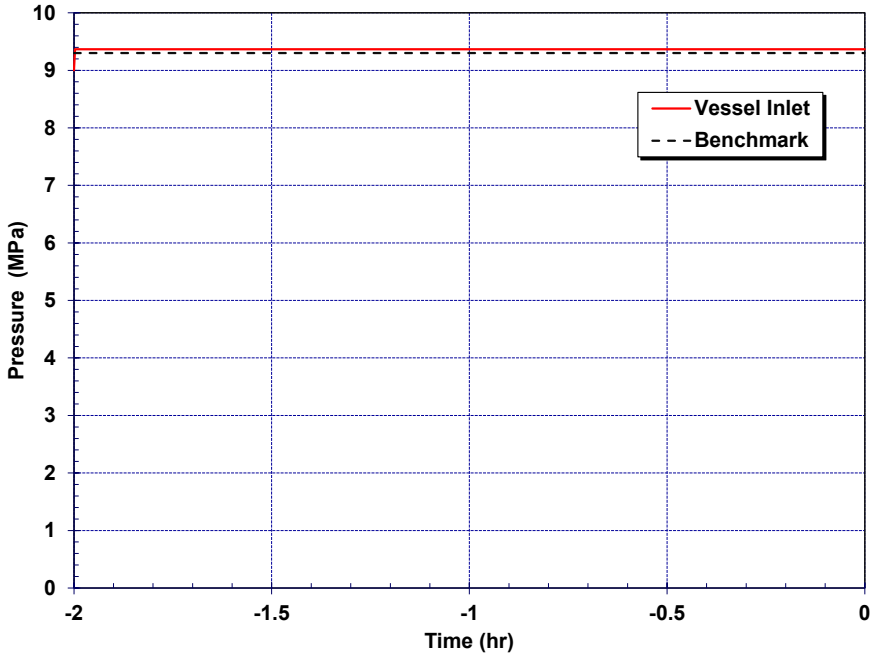

Figure 3-13 Steady state core inlet pressure comparison to the OECD benchmark.

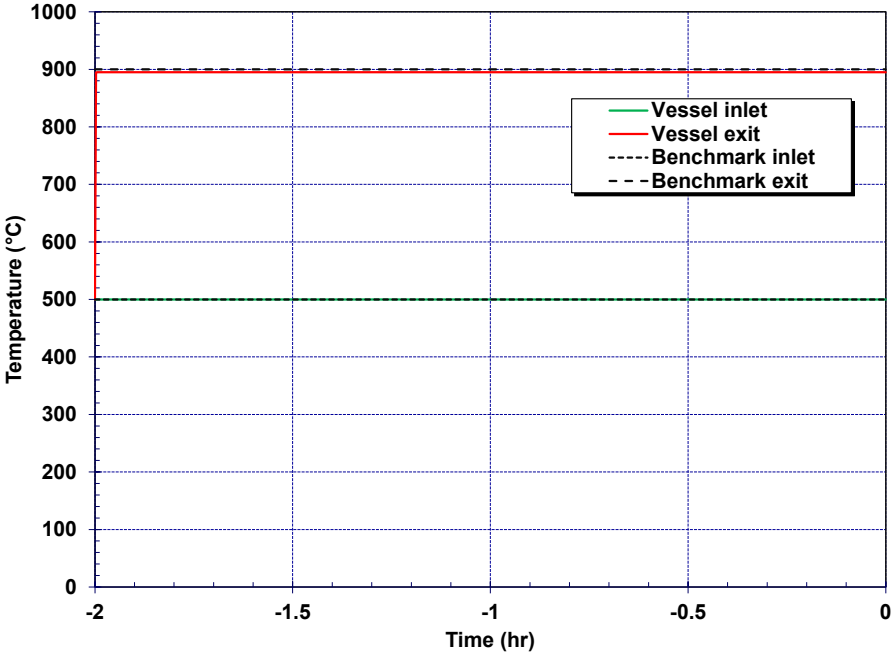

Figure 3-14 Steady state core inlet and outlet temperature comparison to the OECD benchmark.

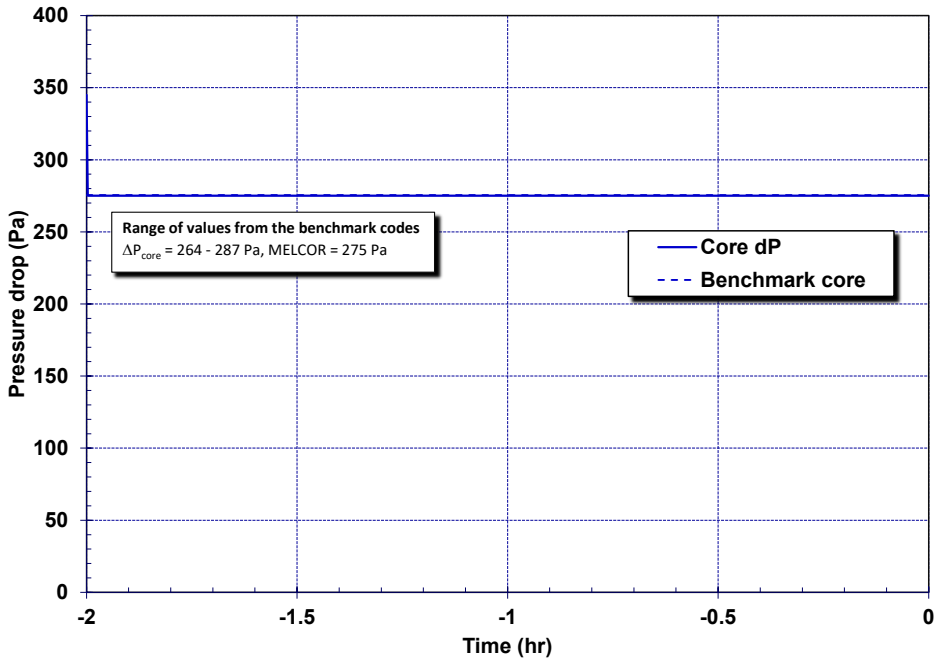

Figure 3-15 Steady state core pressure drop comparison to the OECD benchmark.

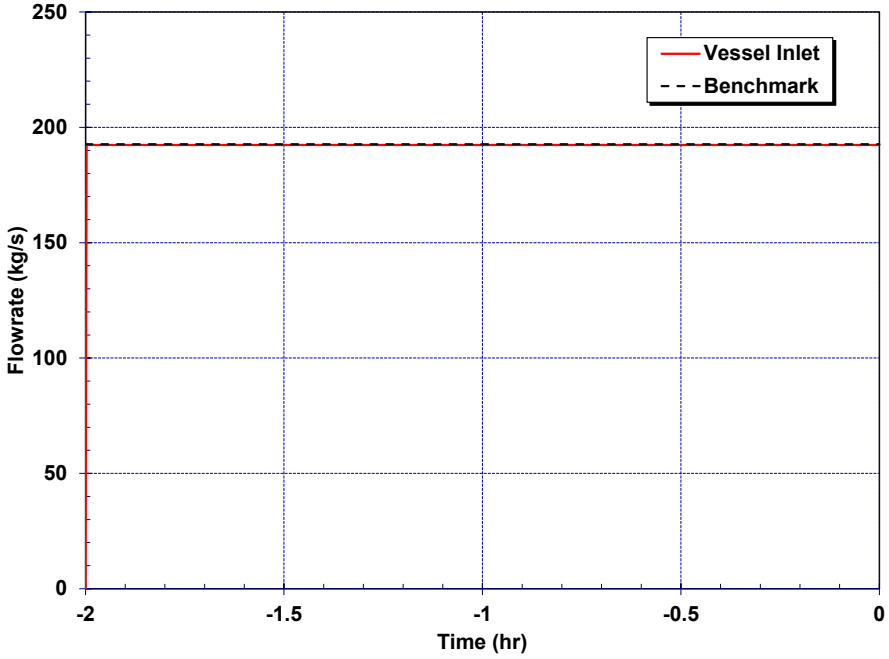

Figure 3-16 Steady state vessel flow comparison to the OECD benchmark.

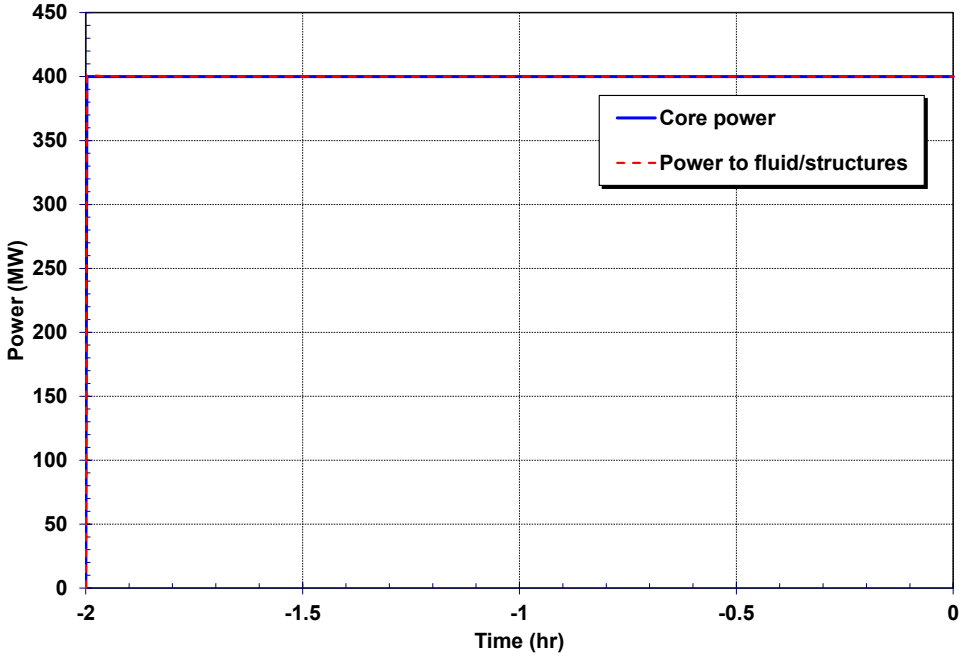

Figure 3-17 Steady state core power.

4. EXAMPLE RESULTS

The PBMR-400 input model was used to perform severe accident simulations that demonstrate MELCOR's HTGR mechanistic source term capabilities for two scenarios. The first scenario is a DLOFC, which was included in the PBMR-400 benchmark exercise. The base case results are described, which is followed by the results of sensitivity calculations with variations in some of the key uncertain parameters. The second scenario is an ATWS and includes station blackout (SBO) with an initial failure of the reactor shutdown system, or an anticipated transient without SCRAM. The base and sensitivity DLOFC scenarios are discussed in Sections 4.1 and 4.2, respectively. The ATWS scenario is discussed in Section 4.3. The discussion of the calculations includes the thermal-hydraulic response of the reactor and the associated radionuclide release behavior.

MELCOR Revision 19798 was used for the DLOFC analysis. The ATWS analysis was performed later and so used an updated version of MELCOR (MELCOR Revision 20811) which included bug fixes. The DLOFC was completed using Revision 19798 as described in this report and presented at the public workshop. The ATWS calculation described in Section 4.3 is a new input model capability and those calculations used a new code version, which had corrections to the accelerated steady state diffusion calculation. As an example of the impact, the cesium release from the TRISO during normal operation (i.e., the accelerated steady state diffusion calculation) is discussed in Appendix A.

4.1. Depressurized Loss-of-Forced Circulation

The DLOFC is initiated with a break of the hot leg piping exiting the reactor vessel (see Figure 3-6). The secondary heat removal system trips offline, the primary system helium circulator trips off, and the reactor protection system inserts the control rods to terminate the fission. The reactor pressure vessel, which is initially at 9.3 MPa, quickly depressurizes to the confinement pressure in <1 min (see Figure 4-1). It is assumed that the reactor confinement building includes a pressure relief pathway that vents the helium gas to the environment. The vent system prevents the over-pressurization damage to the reactor building. The pressure relief system is modeled as dampers that open at high pressure and then subsequently close.

After the primary system blowdown, the flow out the break slows and a natural circulation flow is established into and out of the reactor. The hot leg piping connects to the outlet plenum at the bottom of the reactor and exits horizontally from the reactor vessel (see Figure 3-6). The gases and reflector structures in the reactor exit are very hot, which causes a counter-current flow pattern with hot flow out the top of the broken piping and cooler reactor building confinement air entering through the lower portion of the broken piping. There is also a small flow backwards into the piping towards the secondary heat exchanger on the other side of the pipe break. The flows are very small (±0.025 kg/s) but the flow pattern persists through the end of the simulation (see Figure 4-2).

When the primary system helium circulators are operating, the flow in the reactor is downward from the inlet plenum at the top of the core to the exit plenum (see Figure 3-4). However, after the pipe break, a new pattern is developed inside the vessel. There is an upflow towards the inside of the annular core where the decay heat power is highest and a downflow in the outer periphery of the core where the decay heat power is lower (see Figure 4-3). The radial power profile was provided by ORNL from the SCALE analysis [22]. Similar to the pipe break flow pattern, the flowrates are very small but persistent. The magnitude of the flows are slowed due to the flow resistance in the pebble bed.

At approximately 36 hr, the in-vessel flows increase in magnitude. Prior to 36 hr, the fuel in the reactor core is slowly reestablishing a new temperature profile. During normal operations, the fuel

temperatures increase downward through the core due to the helium circulation flow (see Figure 4-3 at t=0 hr). Due to the high heat capacitance of fuel and the low magnitude of the natural circulation flow, it takes time to invert the fuel temperature profile in the inner portion of the core (see Figure 4-4). Initially the flow was going inverse to the pre-existing temperature gradient in the upflow regions, which limited the circulation rate. The inner three fueled rings of the core had a sustained upflow and the outer ring had a sustained downward flow. However, the fourth fueled ring from the center stagnated near zero flow until 36 hr. The flow increase at 36 hr occurred when the fourth ring's velocity established a downflow comparable to the peripheral ring (i.e., Ring 6, see Figure 3-2). This occurred when the inner three rings overcome the initial inverse temperature gradient (i.e., increasing the magnitude of their flow), which established Ring 5 as downflow region with Ring 6. Both Rings 5 and 6 were lower powered relative to the inner rings and therefore more supportive of a downward flow. The in-vessel natural circulation flow is important because it circulates any released radionuclides from the core to the exit plenum.

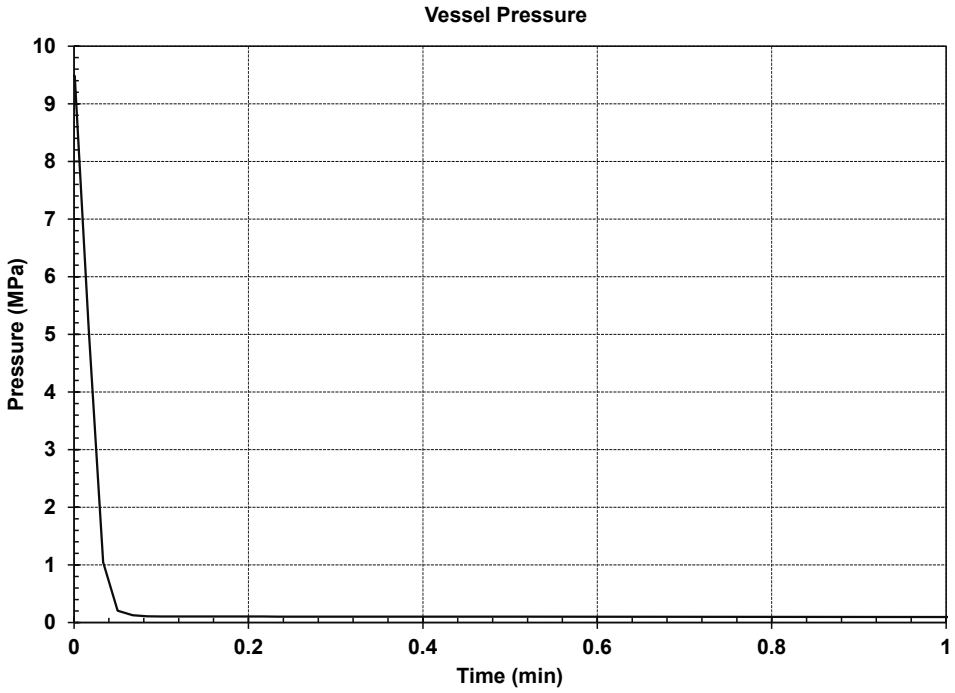

Figure 4-1 Vessel inlet pressure response.

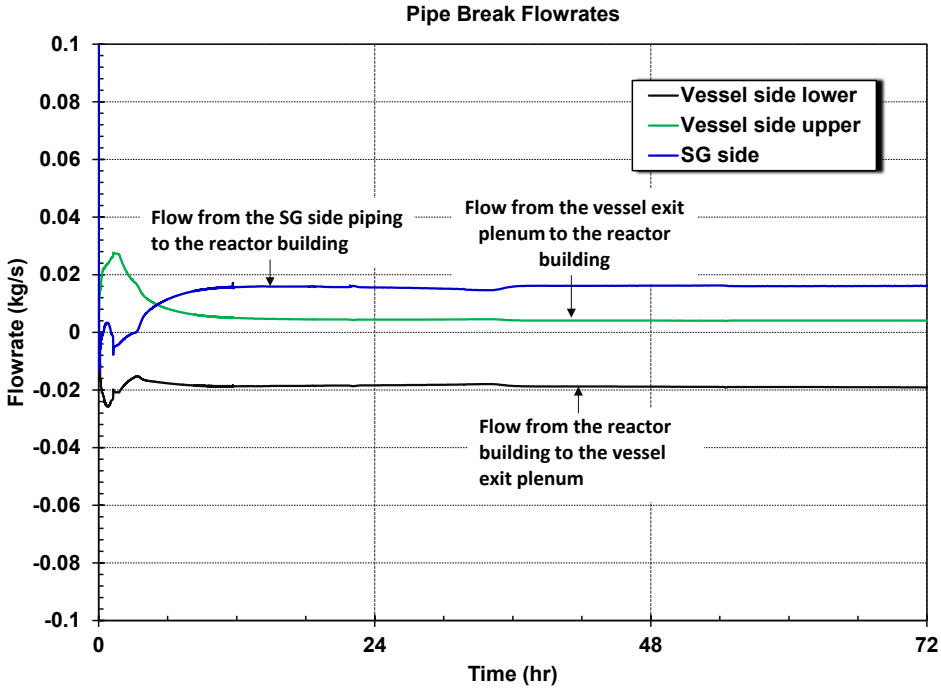

Figure 4-2 Flows in and out of the broken piping.

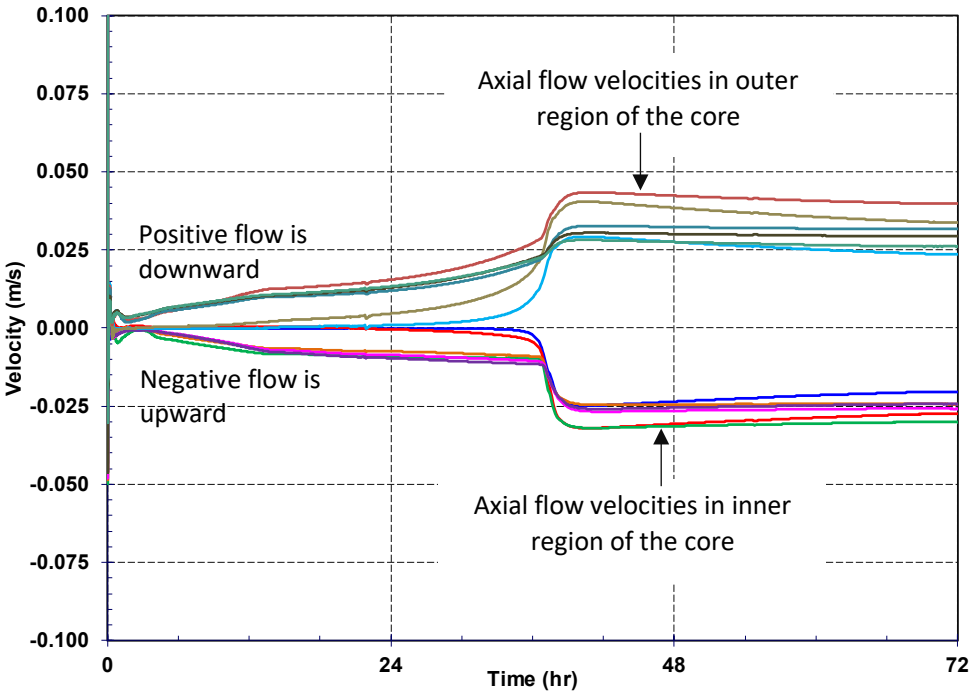

Figure 4-3 Flowrates in the core.

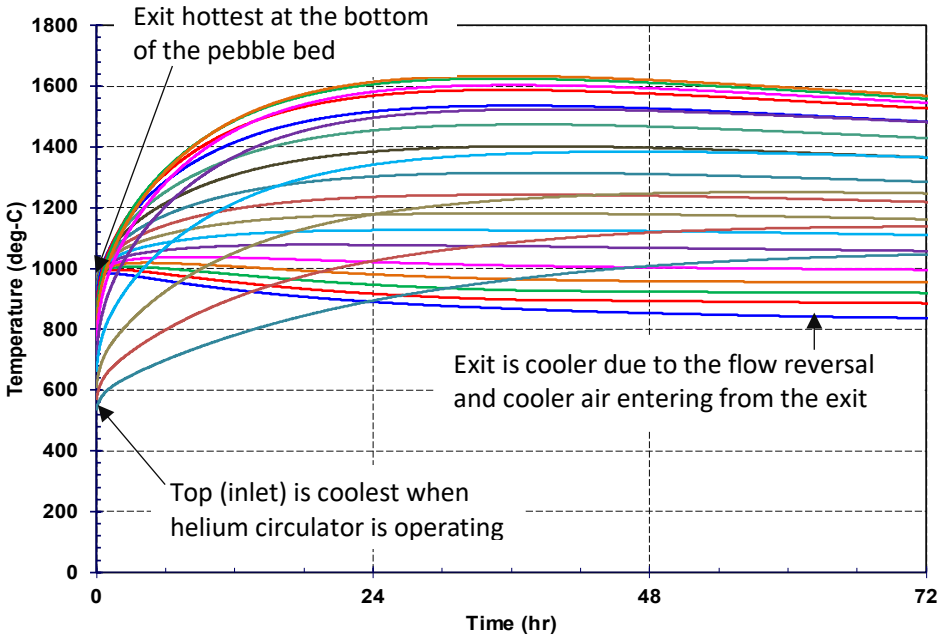

Figure 4-4 Fuel temperature profile in the inner region of the core.

The pipe break flow and in-vessel flow patterns that are shown in Figure 4-2 and Figure 4-3, respectively, are also important for circulating air from the confinement into the vessel. The natural circulation flow pattern at the pipe break causes an ingress of air into the vessel. When the air oxidizes the graphite, there is an exothermic reaction. However, the oxidation heat source is very small relative to the decay heat power (see Figure 4-5). Consequently, the natural flow patterns were not strong enough to create a significant in-vessel oxidation heat source.

MELCOR includes air and steam graphite oxidation models. As discussed previously, the models assume chemical equilibrium for the relative extent of reactions producing carbon-monoxide gas versus carbon-dioxide gas. The results from the DLOFC scenario predicted 794 kg of CO and 271 kg of CO_2 over 72 hr (see Figure 4-6). The gas sources contribute to the flow from the vessel to the reactor building, which can carry radionuclides.

Approximately 50% of the oxidation occurs in the core exit plenum as the air enters the vessel. The core exit plenum oxidation occurs on the large graphite reflector structures. The remaining 50% of the oxygen enters the core through the upflow natural circulation pattern on the inner portion of the pebble bed. The total oxidation mass loss of the fuel pebbles was only 1% but up to 17% where the air entered the inner portion of the core from the exit plenum.

The carbon monoxide and carbon dioxide gases released from the vessel enters and circulates through the reactor building. The carbon monoxide gas is combustible at approximately a 12.9% concentration (i.e., the MELCOR default for the lower combustion threshold for carbon monoxide [8]). In contrast, the released carbon dioxide gas is a dilutant that lowers the building oxygen concentration. The likelihood of combustion is dependent on many factors (e.g., adequate oxygen, an ignition source, oxygen and carbon-monoxide mixing, the connectivity between building compartments, the magnitude of the building natural circulation flows, and non-uniform

concentrations). Due to the relatively low leakage from the building, the carbon monoxide concentration slowly increases but remains below the lower threshold for combustion (see Figure 4-7). There were no burns in the building during the simulation, which was extended to 168 hr.

Like other responses and inputs in the DLOFC demo calculation, the oxidation and combustion phenomena have uncertainties. The potential for combustion in the building is dependent on the rate and magnitude of the carbon-monoxide production, adequate oxygen, the mixing of the carbon monoxide in the air, the production rate of the carbon dioxide diluent, the mixing and circulation patterns between compartments in the reactor building, and the presence of an ignition source. The interconnectivity between compartments in the reactor building was relatively open in the demo model, which promoted good mixing. However, designs could include compartment regions where carbon-monoxide could collect. Furthermore, if a burn should occur, then the pressurization could damage the building and promote a puff release of airborne radionuclides. Uncertainty studies could be performed with MELCOR to explore these parameters to assess the potential and consequences from a burns.

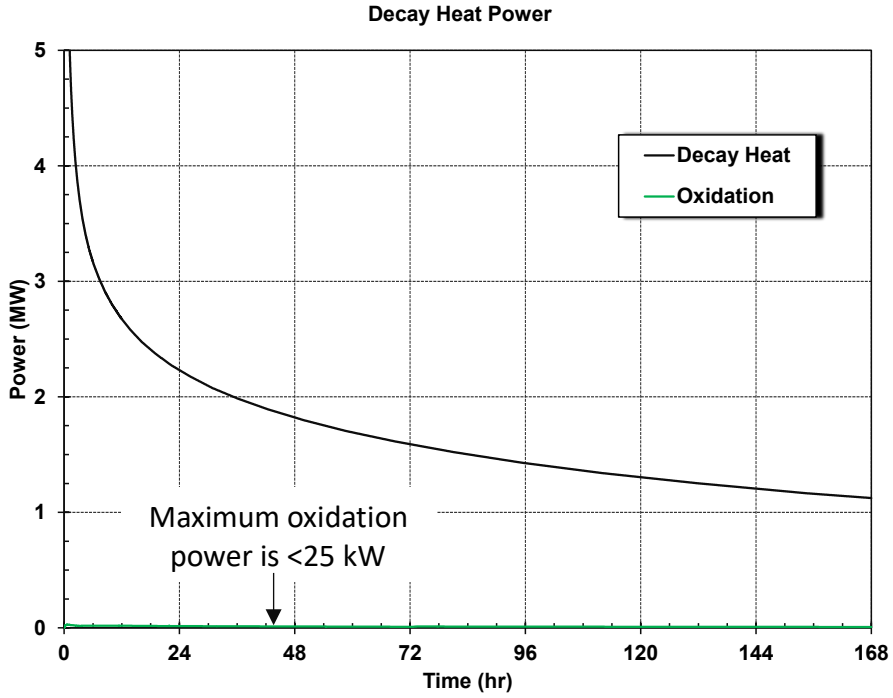

Figure 4-5 Comparison of decay heat and oxidation power.

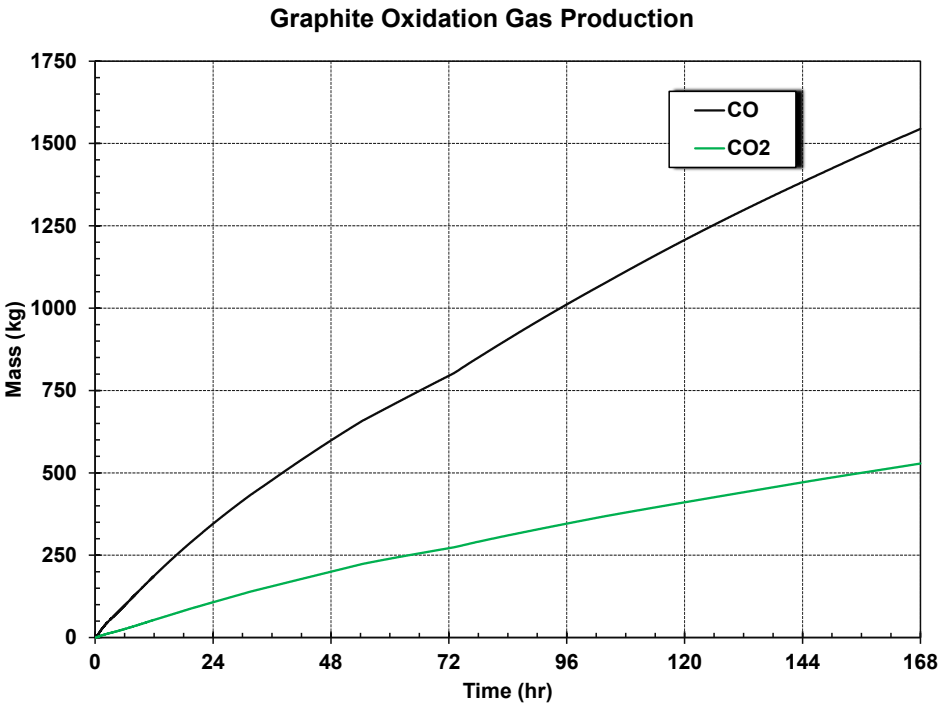

Figure 4-6 Carbon-monoxide and carbon-dioxide production.

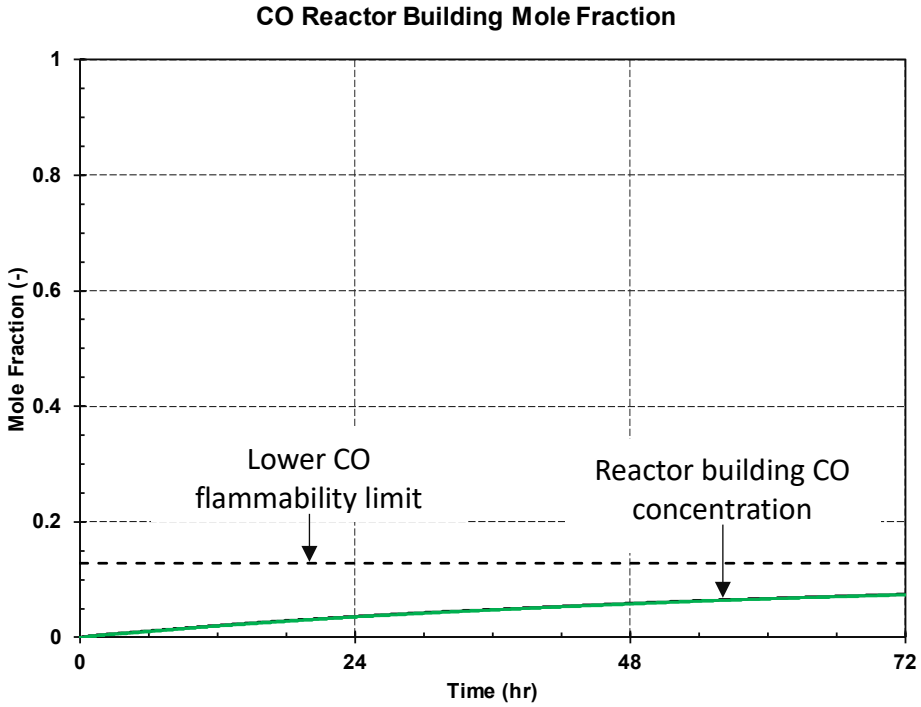

Figure 4-7 Carbon-monoxide and carbon-dioxide mole fractions in the reactor building.

The iodine and cesium release and transport behavior are shown in Figure 4-8 and Figure 4-9, respectively. During the 900-day accelerated steady state phase of the calculation prior to the transient, there are very small releases of radionuclides from the TRISO pebbles into the gas stream.

In addition, graphite dust is generated due to abrasion between the pebbles. The graphite dust and radionuclides are continuously generated but also deposit in the primary circuit. The high velocities during the system depressurization following pipe break causes some of the previously settled aerosols to resuspend and flow out the break. The initial release of iodine and cesium from the vessel into the reactor building and environment is due to the radionuclides already in the primary system at the start of the transient.

Following the pipe break and the loss of the forced circulation cooling, the core heats to a maximum fuel temperature of 1634°C at 35 hr (see Figure 4-10). The TRISO failure model predicts an overall failure fraction of approximately 1.6×10^{-4} by 37 hr, which includes the assumed initial failure fraction of 10^{-5} due to manufacturing defects. The fuel heatup and additional TRISO failures lead to the sustained rise in the cesium releases. In contrast, the iodine release remains relatively low due to the more effective hold up of iodine in the pebbles. However, the release of iodine becomes larger as the fuel reaches the maximum temperature and the iodine diffuses from the failed TRISO through the pebble matrix.

The highest radionuclide release occurred from the silver radionuclides, which also had the highest diffusivity through the intact TRISO silicon-carbide layer at elevated temperatures. The fractional silver release from the fuel was 1.7×10^{-2} at 72 hr, which was two orders of magnitude higher than failed TRISO fraction of 1.6×10^{-4}. Consequently, 99% of the silver releases occurred through the intact TRISO layers to the core gas space at the elevated temperatures during the transient.

The radionuclide distribution results initially show a large hold-up in the vessel (i.e., Figure 4-8 and Figure 4-9 shows the fraction of the initial inventory that leaves the pebble and enters the core gas space). However, the small natural circulation flow steadily transports airborne aerosols into the reactor building. The fractional amount reaching the environment is an order of magnitude lower due to holdup and deposition in the reactor building and the relatively low leakage rate from the reactor building. Both the iodine and cesium distribution results show an increase in the release rate from the vessel to the reactor building between 18 to 36 hr as the core circulation rate increased (see Figure 4-3).

Of the releases of iodine and cesium from the fuel pebbles, 33.6% and 61.7% were retained in the vessel and 57.5% and 34.4% were retained in the reactor building at 7 days, respectively (see Figure 4-11). The small 20.6 cm^2 (3.2 in^2) reactor building leakage area and the low driving pressure for release contributed to the very small environmental releases. Due to the steady exchange between the reactor vessel and the reactor building (see Figure 4-3), the majority of the released radionuclides transported from the vessel to the reactor building. However, the release point from the reactor was to a below-grade compartment in the reactor building. The results show significant hold-up and deposition in the reactor building, which limited the environmental releases.

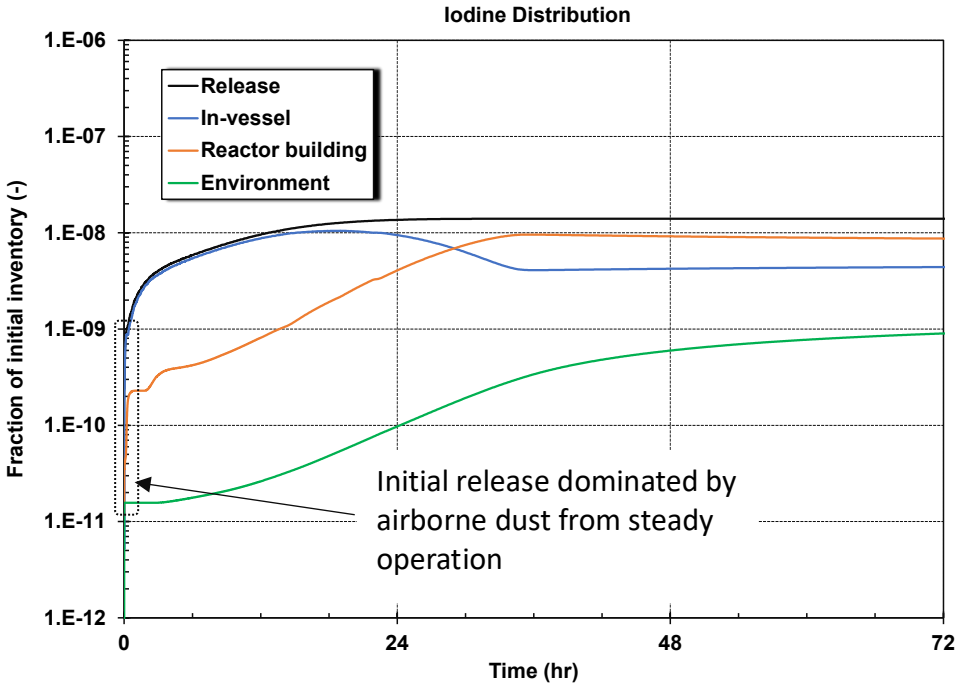

Figure 4-8 Iodine release and distribution.

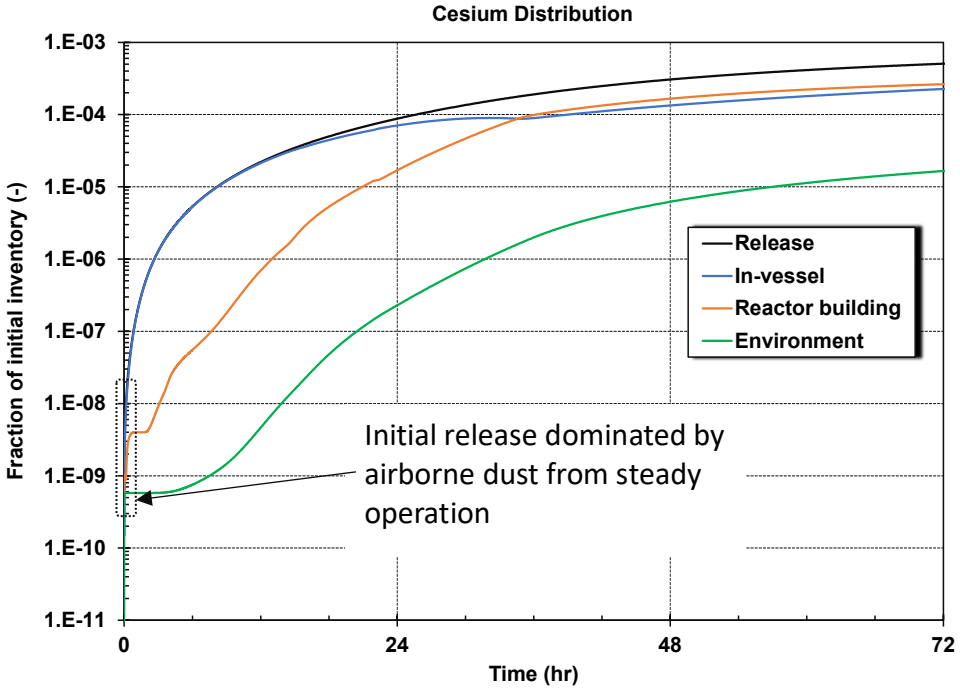

Figure 4-9 Cesium release and distribution.

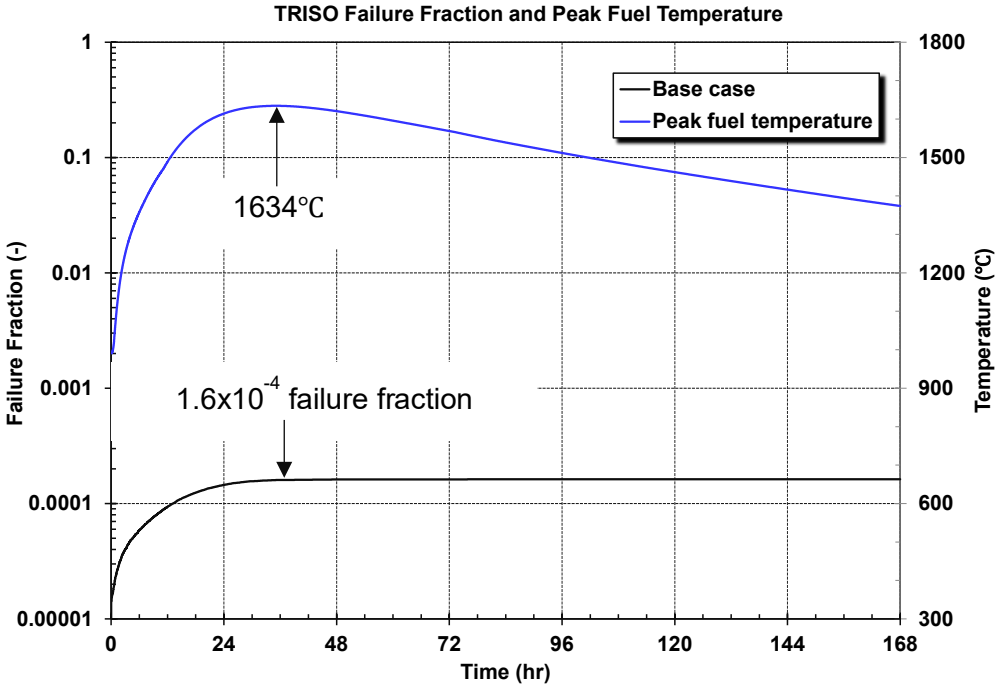

Figure 4-10 TRISO failure fraction and peak fuel temperature.

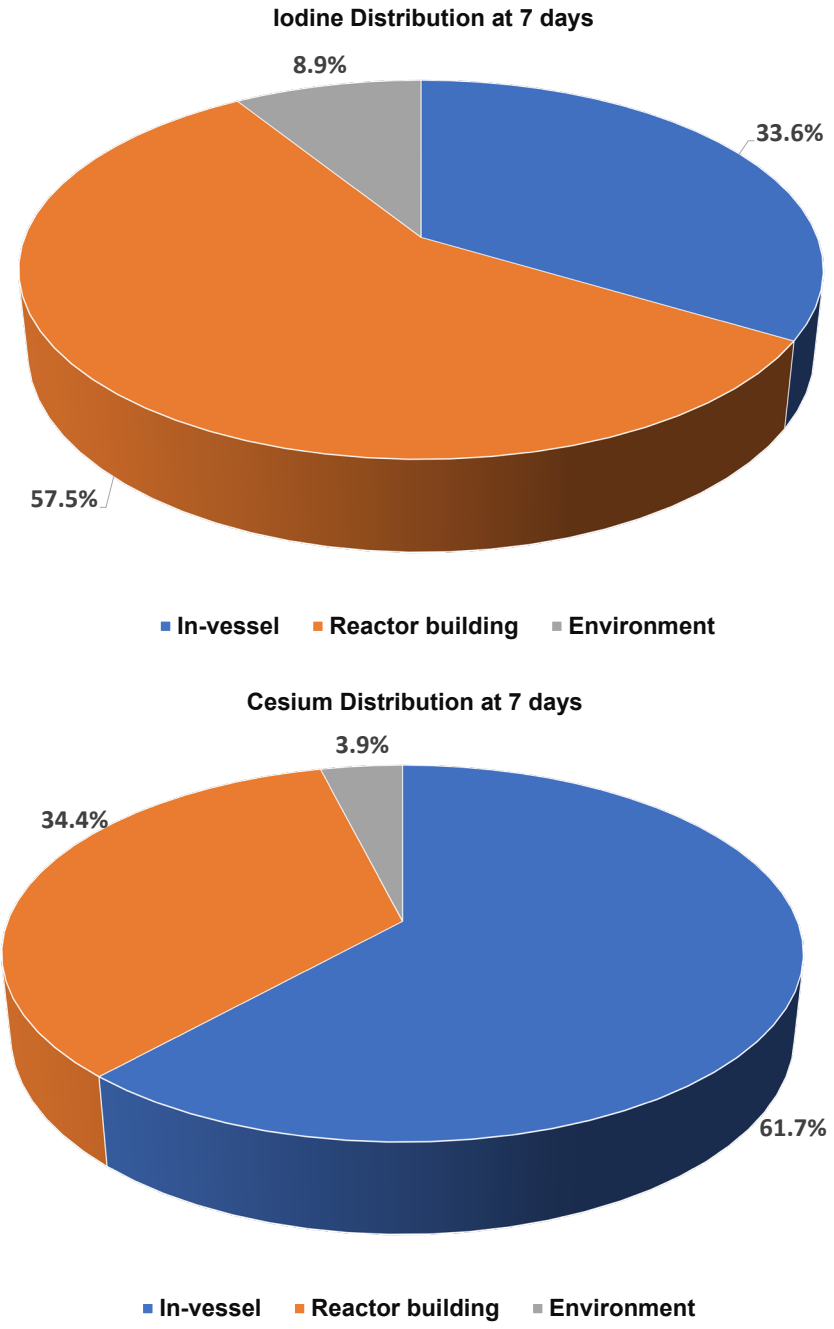

Figure 4-11 Distribution of the released iodine and cesium distribution in the base case.

4.2. Depressurized Loss-of-Forced Circulation Sensitivity Study

MELCOR is well-suited for exploring calculational sensitivities. Many parameters in the physics routines can be sampled and varied in sensitivity calculations. In addition, MELCOR's building block format and control logic allows flexible specification of the uncertain or variable boundary condition parameters. A number of uncertain parameters were identified that could impact the

accident progression or the magnitude of the source term (see Table 4-1). The parameters in the list were not intended to be exhaustive or representative of a formal phenomenon identification and ranking table. Instead, the parameters and their ranges were selected as a preliminary investigation of their impact on key figures of merit, as well as a demonstration of the ability to explore their importance in the source term calculation. The following examples varied one parameter at a time at their maximum and minimum. However, the next logical application is a Monte Carlo uncertainty sampling of all uncertain parameters simultaneously. A MELCOR Monte Carlo uncertainty analysis was performed as part of this project. The results of the uncertainty analysis are described in the public workshop slides [5]).

The peak fuel responses of some key uncertain parameter calculations impacting the in-vessel temperature response are shown in Figure 4-12. The most significant parameter affecting the peak fuel temperature was the graphite thermal conductivity. The efficiency of the radial conduction through the pebble bed and radial reflectors has an important impact of the core temperature response, which is strongly impacted by the graphite thermal conductivity. There is active research and development of reactor grade graphite, which is also identified as an important parameter in an HTGR phenomena identification ranking assessments (e.g., [23]). For example, the graphite thermal conductivity varies considerably due to irradiation, the grade, and with temperature. A 50% reduction in the graphite thermal conductivity had the largest impact on the peak fuel temperature.

A 10% increase in the decay heat had the next largest impact, which was followed by the pebble bed graphite emissivity. The emissivity of the graphite was varied to 0.5 to 0.99 versus the base value of 0.9. Although it is an important parameter in the combined radiative and conductive pebble bed radial heat transfer, the large variance did not show a dominant effect. The pebble bed porosity (i.e., ±0.1) also had a relatively small impact on the combined conduction and radiation pebble bed heat transfer.

If the RCCS is unavailable, then there is limited convective heat removal from the vessel. The dotted brown curve in Figure 4-12 shows the extreme case of no RCCS heat removal (e.g., blocked). The initial results through 48 hr show that the graphite core is effective at dissipating heat from across the core and limiting the initial peak temperature. However, the lack of the passive heat removal eventually results in a slow heat-up of the fuel in the core. The response illustrates the effectiveness of the initial heat dissipation phase from the fuel in the pebble bed to the surrounding graphite reflectors. The peak temperature is less than 1800°C at 168 hr (7 days).

Another key indicator of the magnitude of the radionuclide release from the fuel is the TRISO failure fraction. As shown in Figure 2-1, the radionuclides from a failed TRISO go into the pebble matrix. The failure (e.g., cracking due to the internal thermal and gas generation pressurization) opens a pathway for radionuclides from the TRISO fuel kernel to the pebble matrix, which has a more limited retention effectiveness. The overall core TRISO failure fraction is shown Figure 4-13. The results are consistent with the peak fuel temperature trends in Figure 4-12, which was expected due to the temperature-based formulation for the failure correlation (see Figure 3-11).

The TRISO failure curve results also show about an order of magnitude increase in failures above the assumed initial failure fraction of 10^{-5} for most uncertain parameter calculations (i.e., especially for uncertain values that reduce the change). However, as noted in the peak fuel temperature response, the low graphite thermal conductivity case, the higher decay heat, and the lower pebble emissivity had larger TRISO failure fractions but only twice as large as the base case. The blocked RCCS eventually has the largest increase in the TRISO failure fraction after 5 days and ~3.5 larger than the base case at 168 hr.

Figure 4-14 and Figure 4-15 show the impact of the uncertain parameters on the iodine and cesium release from the pebbles to the core gas space, respectively. Neither the iodine nor the cesium release from the pebbles show a large variation versus uncertain parameters. The iodine release follows the TRISO failure fraction response and slowly builds up from the initial release from 900 days of normal operation to the peak accident values. Since the low graphite thermal conductivity case reaches a higher temperature and cools more slowly, the thermal effects impacting the iodine diffusivity through the matrix show a sustained impact through 168 hr, albeit very small in absolute magnitude.

Next, the impact of the uncertain parameters on the environmental release are shown in Figure 4-16 and Figure 4-17. As previously shown in Figure 4-8 and Figure 4-9, the environmental release is small relative to the release from the pebbles. The variations of the environmental releases versus the various uncertain parameters are about an order of magnitude. Only the iodine release in the low graphite thermal conductivity case is slightly larger than an order magnitude larger than the lowest result (see Figure 4-16).

The environmental releases generally follow the releases from the pebbles but include significant hold-up in the reactor vessel and the reactor building. For reference, the distribution of the iodine and cesium in the base case is shown in Figure 4-11. Only 8.9% and 3.9% of the released iodine and cesium reached the environment within 7 days. The iodine release is slightly higher than the cesium release due to 5% of the iodine assumed to be in a gaseous form that does not settle. In contrast, all of the released cesium is transported in an aerosol form, which can settle in the reactor vessel or the reactor building.

Other factors could impact the magnitude of the environmental release. Some of these factors include the leak tightness of the reactor building, the interconnectivity between the compartments, an external wind, and a combustion pressurization. Figure 4-18 and Figure 4-19 show the iodine and cesium environmental release results, respectively, that highlight a few of these impacts. The reactor building leakage was scaled by 10X and 100X; an external wind of 10 m/s was applied; and the final case is an event that blocked the RCCS passive heat removal. The increased reactor building leakage results show up to an order of magnitude larger release, which is an order of magnitude smaller than the scale factor on the building leakage. As shown in the figures, the increased leakage is more important in the first 48 hr than in the last 120 hr. There are competing effects of aerosol settling that attenuate the magnitude of the release versus the higher leak area. Consequently, the difference in the 100X and 1X leakage cases is less one order of magnitude at 168 hr.

There is a low driving force for leakage in the DLOFC scenario. Consequently, an external wind may increase leakage due to variations in the Bernoulli pressure forces on the building. A 10 m/s wind increases the infiltration on the upwind side of the building and increases the exfiltration on the downwind side of the building. The wind has a small effect on the magnitude of the environmental release.

Finally, the blocked RCCS result is also shown on the figures. The blocked result shows slightly more iodine and cesium hold-up in the reactor building until a carbon-monoxide burn at 145 hr. The hold-up is attributed to small changes in the internal vessel and break flow patterns that promote a slightly lower exchange to the reactor building. The blocked RCCS retained more heat in the vessel, which slightly limited the magnitude of the in-vessel natural circulation and the exchange with the reactor building.

The higher vessel temperatures also promoted more oxidation (i.e., the oxidation rate increases with temperature). Figure 4-20 shows a comparison of the carbon-monoxide and carbon dioxide

production in the base case and the blocked RCCS case. Not only did the higher temperatures in the blocked RCCS case increase the total gas production, but the higher temperatures also increased the carbon monoxide production relative to the carbon dioxide production, as included in the oxidation modeling [8]. The carbon monoxide concentration reached the lower flammability limit for combustion at 145 hr and a burn was predicted . The burn was predicted in the steam generator compartment where the pipe break is located. However, the impact on the release was relatively minor as shown Figure 4-18 and Figure 4-19. If the burn occurred in the above-grade compartment or caused structural building damage, then the impact could have been greater.

Table 4-1 Uncertain parameters for the PBMR-400.

Model	Parameter	Distribution **	Range
TRISO Model Parameters	Initial TRISO Failure Fraction (fraction of inventory)	Log uniform	10^{-6} – 10^{-4}
	TRISO Failure Rate Multiplier (-)	Log uniform	0.1 – 1.0
	Intact TRISO Diffusivity Multiplier (-) *	Log uniform	0.01 – 100
	Failed TRISO Diffusivity Multiplier (-) *	Log uniform	0.01 – 100
	Matrix Diffusivity Multiplier (-) *	Log uniform	0.01 – 100
	TRISO Pebble Emissivity (-)	Uniform	0.5 – 0.999
	TRISO Pebble Bed Porosity (-)	Uniform	0.3 – 0.5
	TRISO recoil fraction (-)	Uniform	0 – 0.03
Radionuclide Model Parameters	Shape Factor (-) *	Uniform	1.0 – 5.0
	Gaseous Iodine Multiplier (Base = 5% I_2) *	Uniform	0.02 – 1.0
Design Parameters	Graphite Thermal conductivity Multiplier (-)	Uniform	0.5 – 1.5
	Decay Heat Multiplier (-)	Uniform	0.9 – 1.1
	RCCS Blockage Multiplier (-)	Log uniform	0.001 – 1.0
	RCCS Emissivity (-)	Uniform	0.1 – 1.0
	Reactor Building Leakage Multiplier (-)	Log uniform	0.1 – 100
	Wind speed (m/s)	Uniform	0 - 10

* Not sampled in the sensitivity study.
** Linear or log-linear distributions are specified to survey the full range without bias.

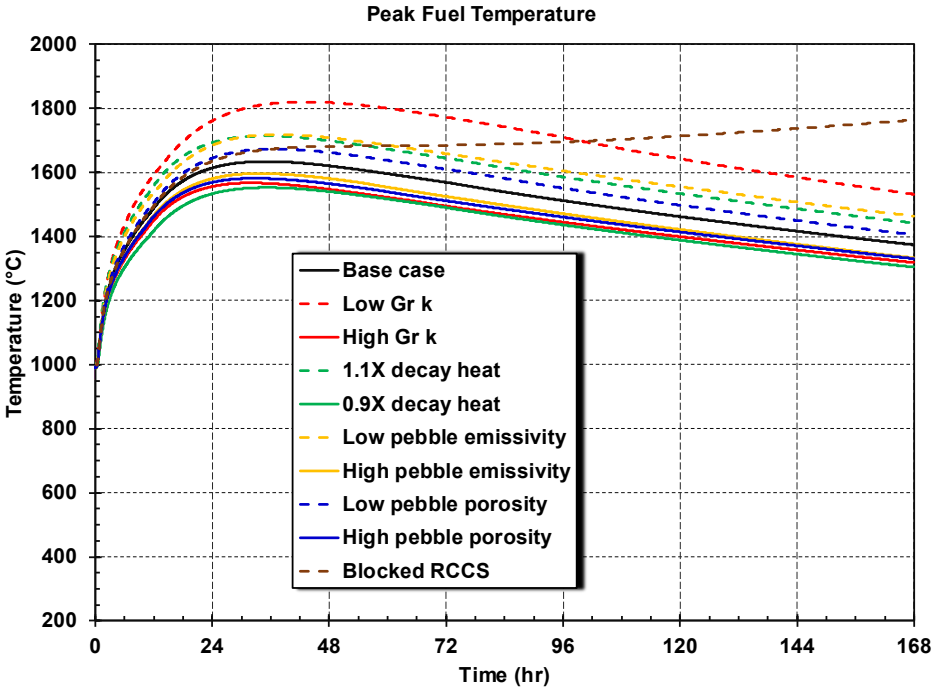

Figure 4-12 Uncertain parameter impact on the peak fuel temperature.

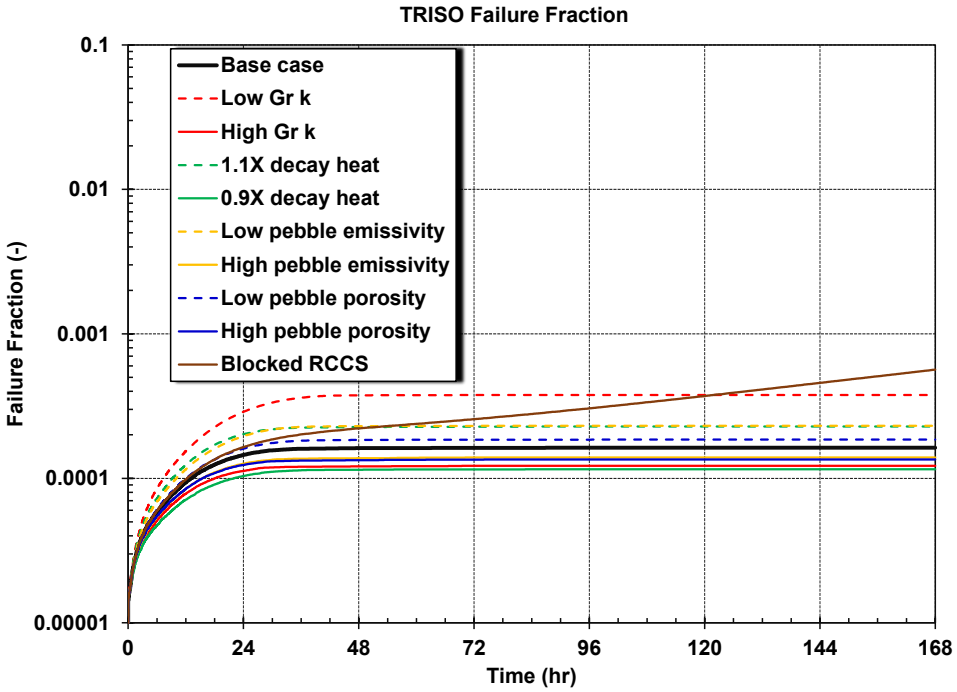

Figure 4-13 Uncertain parameter impact on the TRISO failure fraction.

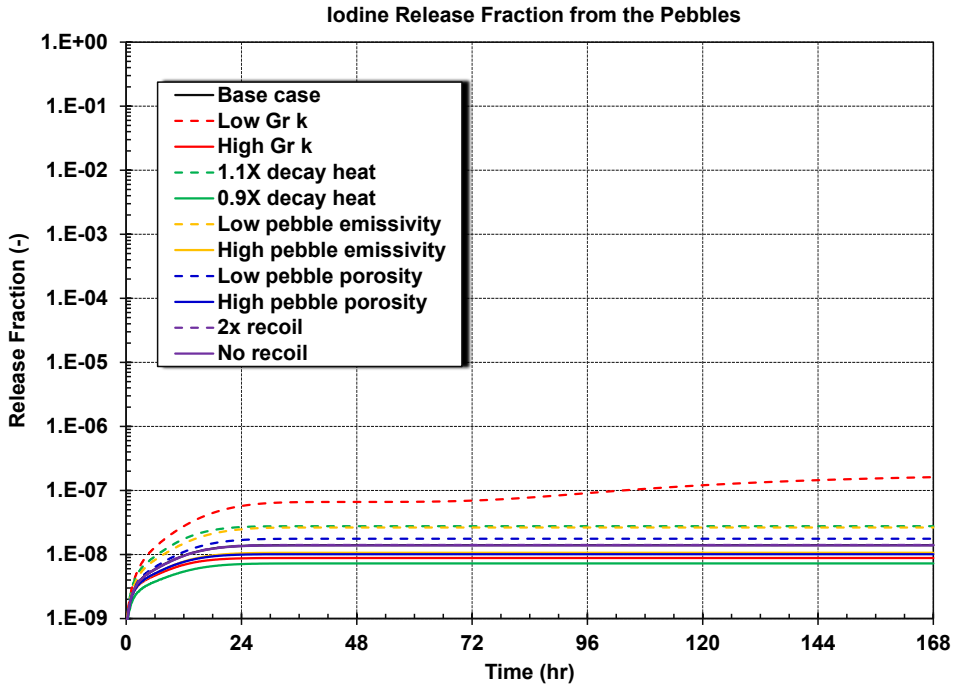

Figure 4-14 Uncertain parameter impact on the iodine release from the pebbles.

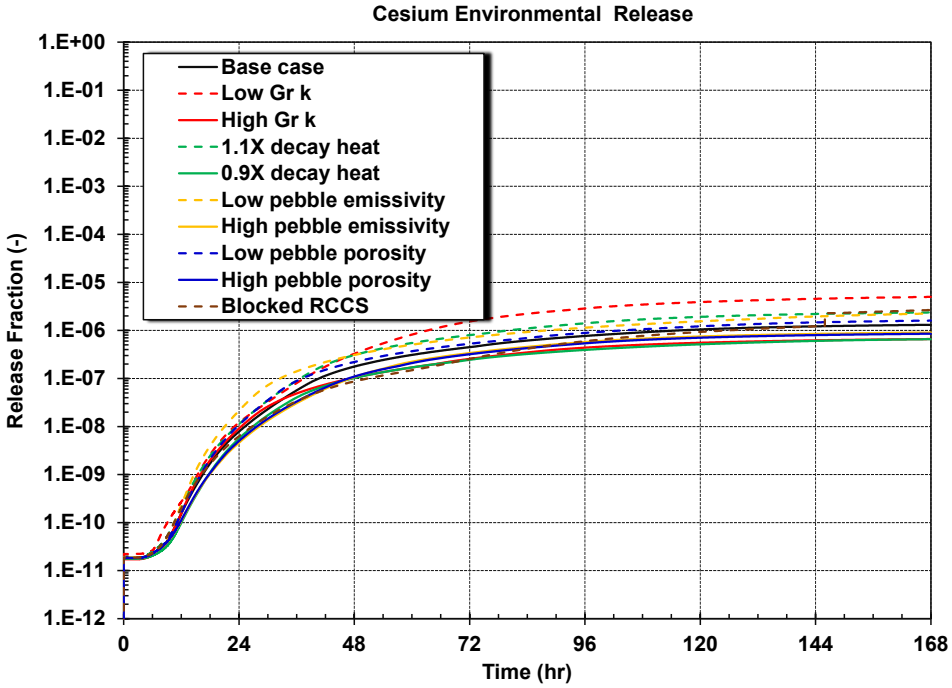

Figure 4-15 Uncertain parameter impact on the cesium from the pebbles.

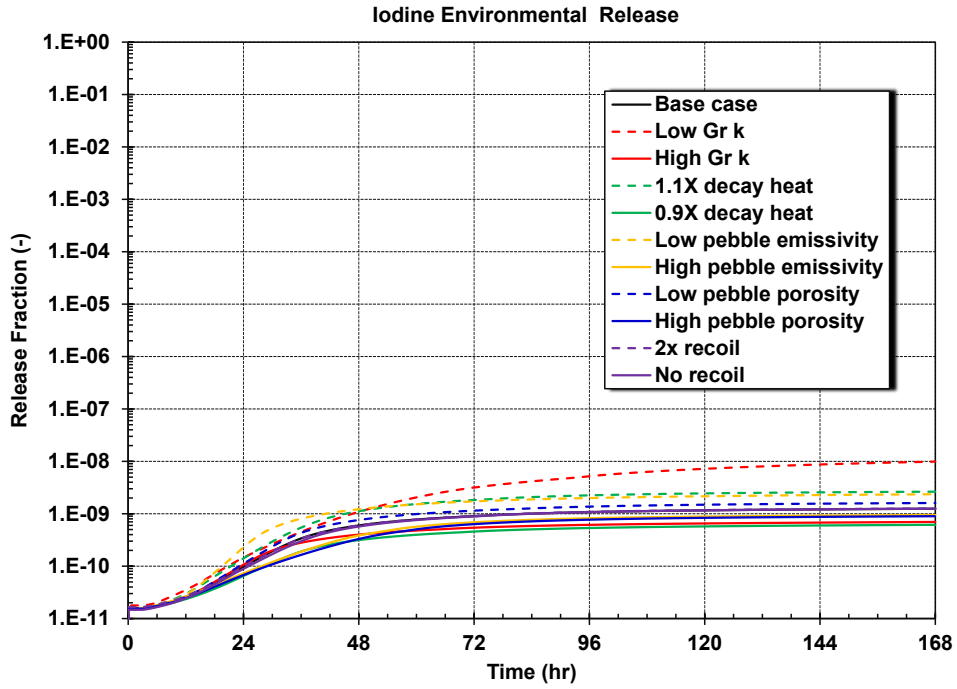

Figure 4-16 Uncertain parameter impact on the iodine release to the environment.

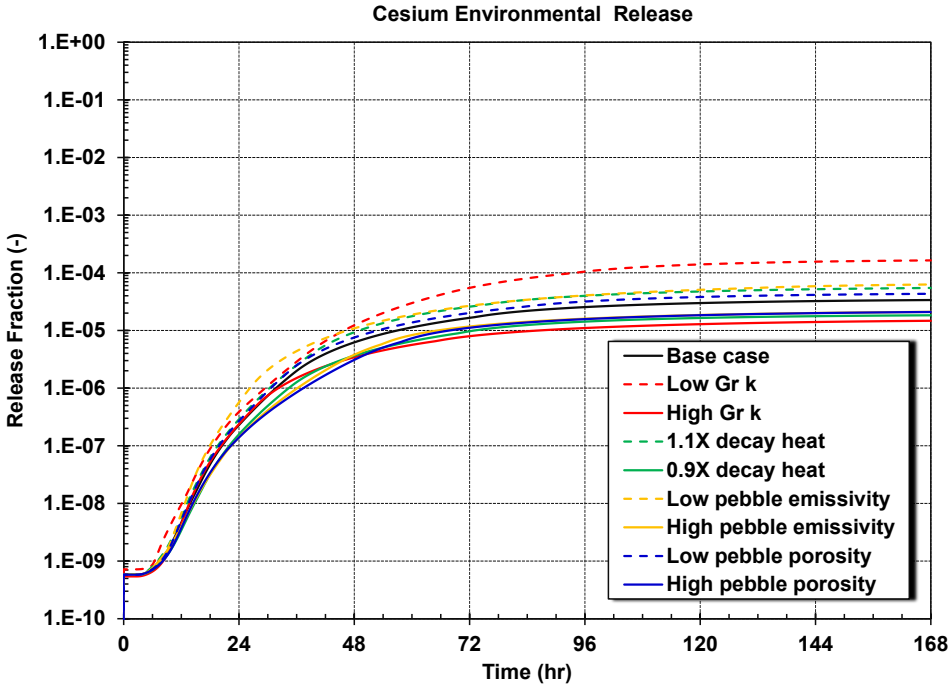

Figure 4-17 Uncertain parameter impact on the cesium release to the environment.

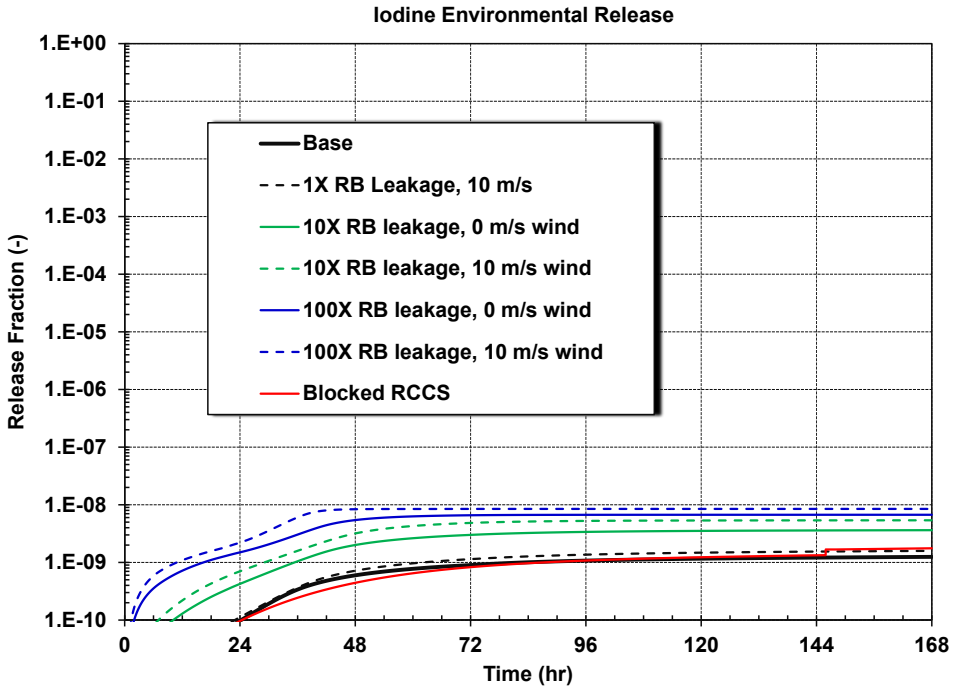

Figure 4-18 Reactor building uncertain parameter impact on the iodine release to the environment.

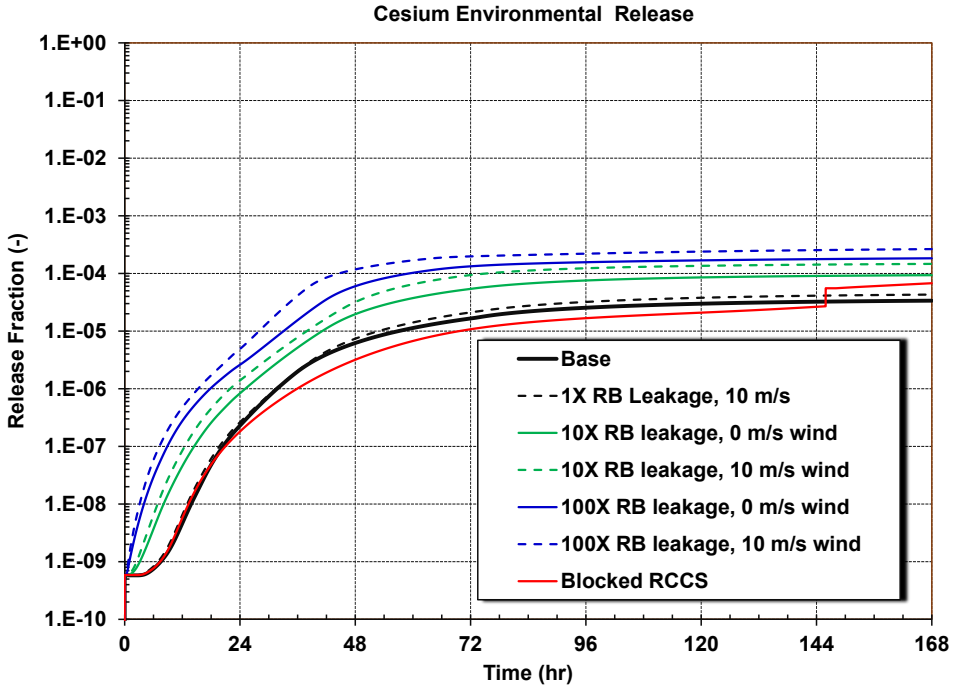

Figure 4-19 Reactor building uncertain parameter impact on the cesium release to the environment.

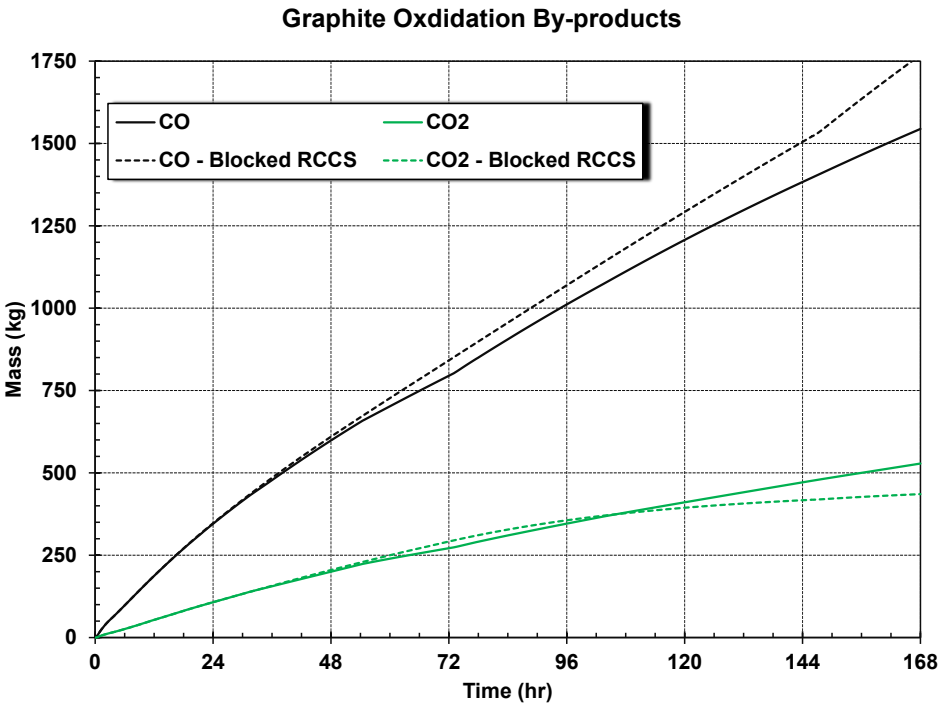

Figure 4-20 Comparison of the base case and blocked RCCS oxidation gases.

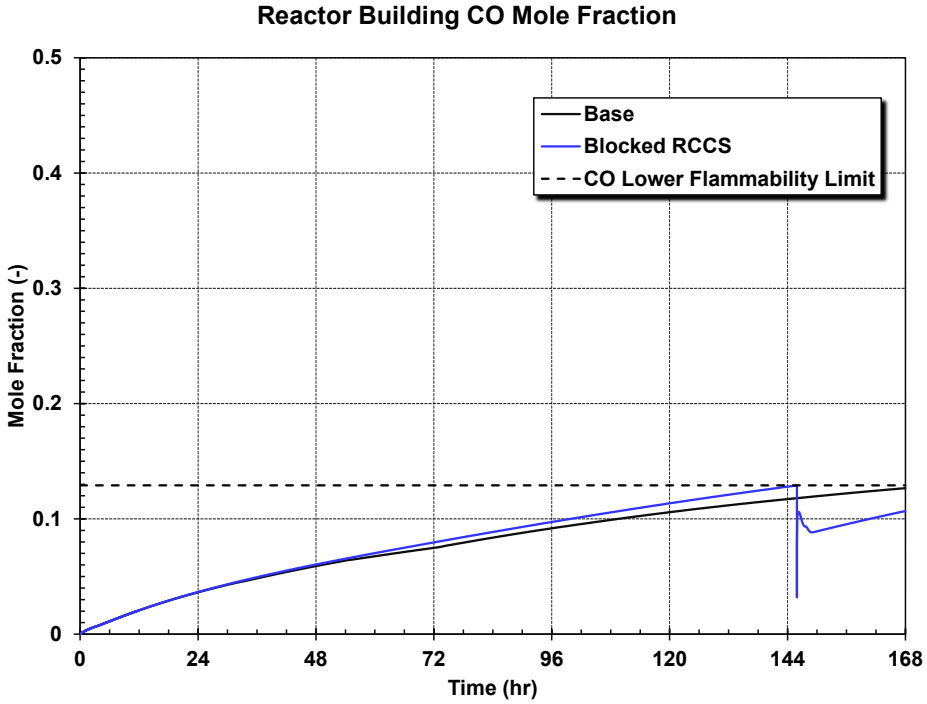

Figure 4-21 Comparison of the base case and blocked RCCS reactor building carbon monoxide mole fraction.

4.3. Anticipated Transient Without SCRAM

An anticipated transient without SCRAM (ATWS) accident was simulated to demonstrate MELCOR simulation capabilities for events involving reactivity feedback. The initiating event was a trip of both the primary system helium circulator and the secondary system air circulator. Figure 4-22 shows a steady decrease in the reactor power from 400 MW to decay power levels by 289 sec (see Figure 4-22). The decrease in the core power is in response to the negative doppler and fuel density reactivity feedback due to the increase in the average fuel temperature. The decay power is assumed to be unchanged until the fission power approaches zero as an analysis simplification. After the fission power diminishes to a small value, the decay power is specified to decrease at the post-SCRAM rate.

The combined Doppler and fuel density feedback is negative as the average fuel temperature rises from the normal operating temperature (818°C) to a peak of 968°C at 1600 sec (26.7 min), as shown in Figure 4-24. Although the fuel responds relatively quickly to the loss of heat removal and flow, there is inadequate time for any significant amount of heat transfer to the large reflectors. Consequently, the moderator feedback has a negligible impact to shut down the fission reaction. Well after the end of any significant fission power, the reflector feedback starts to provide additional negative feedback as the reflectors heat up after 1000 sec.

A third feedback is approximated in this example calculation, which is xenon poisoning. The xenon poisoning transient introduces a strong negative reactivity due to its large cross-section for neutron capture. The xenon poisoning response could be supplied by SCALE but was not part of the data requested or supplied from ORNL (i.e., the demonstration calculation focused on the DLOFC sequence). In lieu of a xenon reactivity response from SCALE, the xenon feedback from Reference [24] for a similar transient was digitized and added to the model to include this phenomenon. Following the decrease in power from 400 MW to only decay heat power, the xenon builds up due to the decay of I-135 to Xe-135. The Xe-135 concentration reaches a peak in about 10 hr and takes another 20 hr to decay back to the previous full-power level [24].

The long-term average fuel and moderator reflector temperatures are shown in Figure 4-24. Over time, the heat from the core transfers to the large reflectors and finally to the RCCS. As the outside of the vessel heats, the heat transferred to the RCCS gradually increases to about 1.3 MW by 24 hr. The overall response illustrates how the radial heat dissipation to the reflectors mitigates the magnitude of the core heatup until the decay heat starts to approach the RCCS heat removal capacity. The RCCS heat removal is estimated to match the decay heat generation at approximately 4 days.

The peak fuel temperature was 1203°C at 3640 sec (60.7 min), which led to a 4.2×10^{-5} average fractional failure of the TRISO (see Figure 4-25). Due to the modest temperature rise, the average TRISO failure rate was close to the initial value of 1×10^{-5}. The average number of failures stabilizes at this value once the average fuel temperature starts to decrease.

The calculation was terminated at 100,000 sec (27.8 hr) with the combined Doppler and fuel density, Moderator, and xenon poisoning feedbacks still combining to provide a strong negative feedback. If the control rods were not inserted during this time, the reactor will return to power after the xenon feedback stopped offsetting the other feedbacks (e.g., after 55 hr as reported in Reference [24]). This portion of the calculation was not simulated.

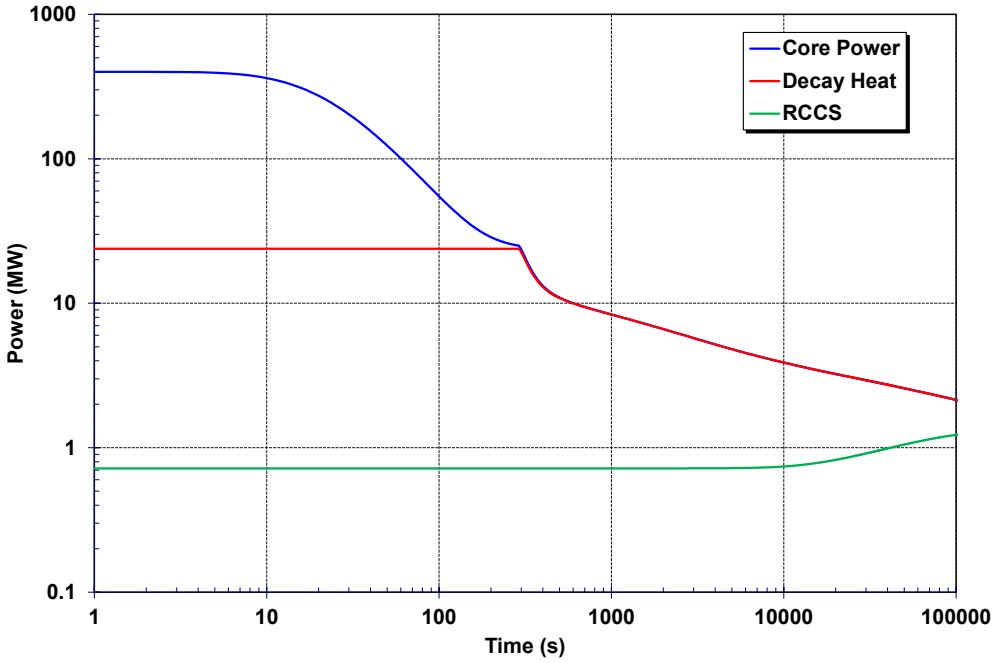

Figure 4-22 Core power and RCCS response in the ATWS.

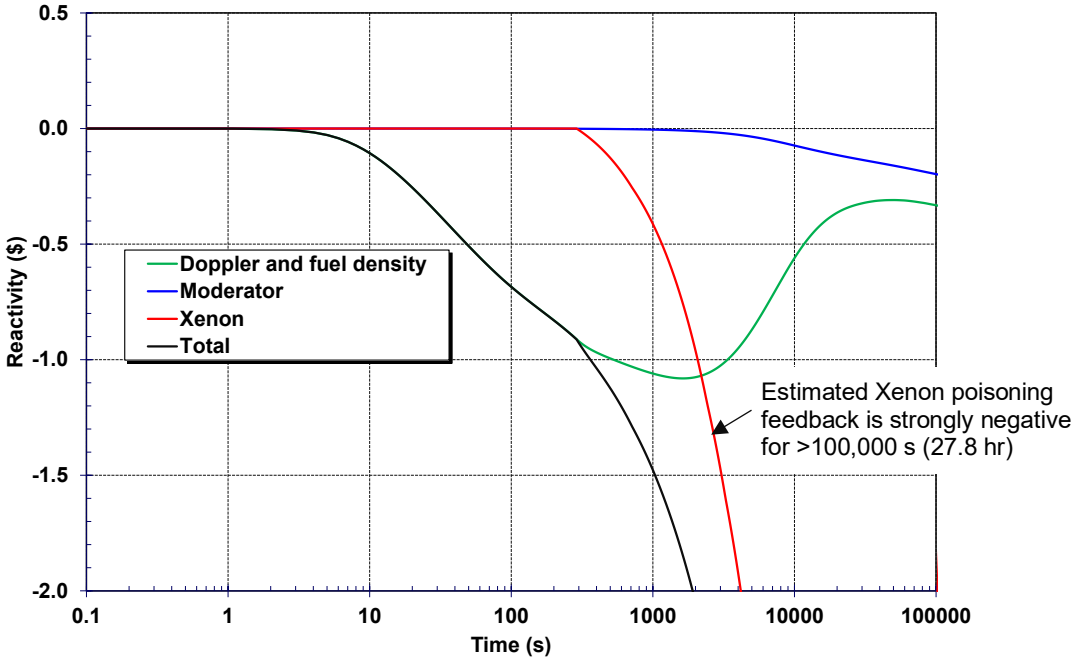

Figure 4-23 Average Doppler, moderator, and xenon feedback in the ATWS.

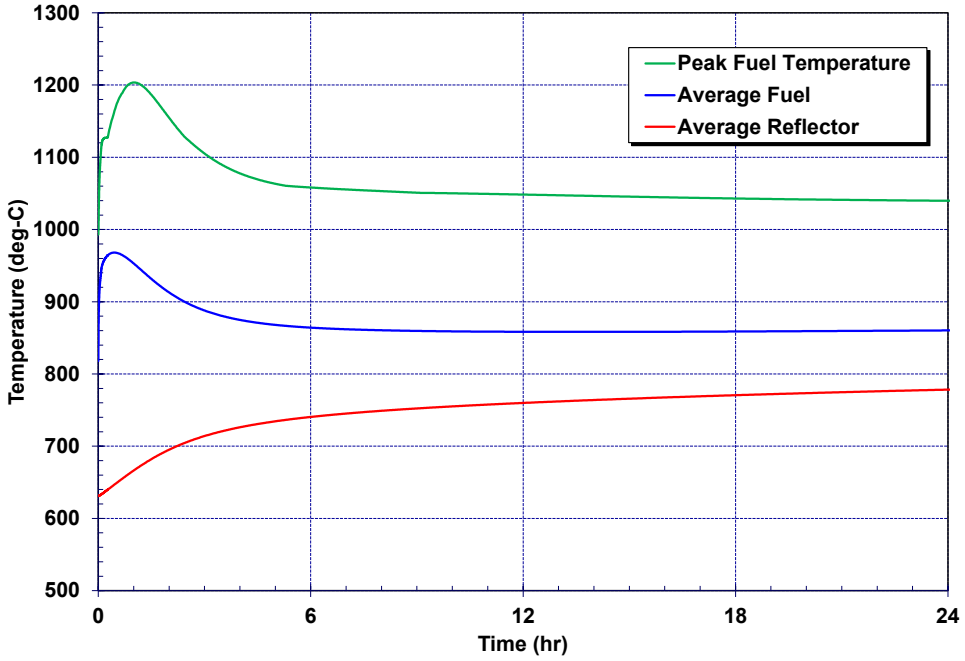

Figure 4-24 Average fuel and reflector feedback in the ATWS.

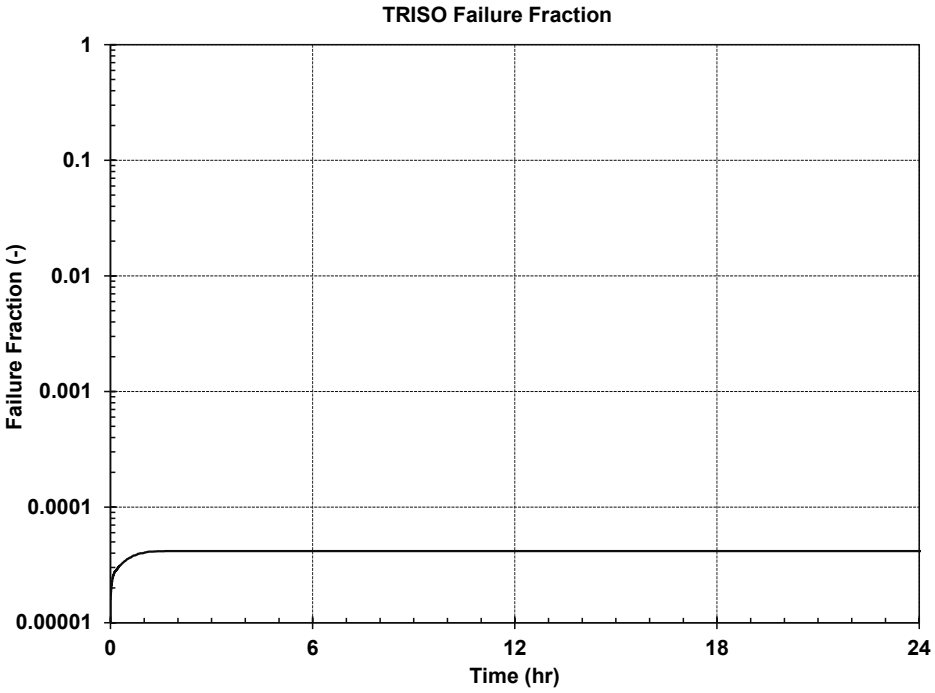

Figure 4-25 Average TRISO fraction in the ATWS.

5. SUMMARY

The MELCOR code has been updated to support NRC safety evaluations of accidents in HTGRs. This report presents demonstration calculations for a HTGR from publicly available literature for PBMR-400. For plant aspects (e.g., reactor building size and leak rate) that are not described in the PBMR-400 references, the analysts made assumptions needed to construct a MELCOR full-plant model. A model of the PBMR-400 was developed to demonstrate a mechanistic source term analysis, which included the vessel with the pebble bed core, the helium circulation system and secondary heat exchanger, and the reactor building. The PBMR-400 input model was used to demonstrate the analysis of the DLOFC accident and the associated source term. Sensitivity calculations were performed on some of the uncertain inputs to illustrate the code's response to these variations. A second scenario without SCRAM was performed to illustrate capabilities to simulate reactivity transients. The analyses demonstrate the flexible capabilities of MELCOR to evaluate the accident progression in a HTGR. The code can incorporate evolving data from ongoing research programs and includes flexible inputs for sensitivity and Monte Carlo sampling on uncertain parameters. While a pebble bed reactor is demonstrated here, the code includes comparable models for a prismatic TRISO fuel design.

REFERENCES

[1] "Non-LWR Vision and Strategy Near-Term Implementation Action Plans," Nuclear Regulatory Commission, ADAMS Accession No. ML16334A495, 2019.

[2] "Nuclear Energy Innovation and Modernization Act," Public Law No: 115-439, January 2019.

[3] B. Rearden and M. Jessee, "SCALE Code System, ORNL/TM-2005/39, Version 6.2.3," UT-Battelle, LLC, Oak Ridge National Laboratory, 2018.

[4] Corson, James Robert, "Development of MELCOR Input Techniques for High-Temperature Gas-Cooled Reactor Analysis," https://oaktrust.library.tamu.edu/handle/1969.1/ETD-TAMU-2010-05-7940, May 2010.

[5] "SCALE/MELCOR Non-LWR Source Term Demonstration Project – High-Temperature Gas-cooled Reactor," NRC Adams Ascension Number ML21200A179, https://www.nrc.gov/docs/ML2120/ML21200A179.pdf, July 2021.

[6] "PBMR Coupled Neutronics/Thermal-hydraulics Transient Benchmark - The PBMR-400 Core Design," NEA/NSC/DOC(2013)10, July 2013.

[7] F. Reitsma, K. Ivanov, T. Downar, H. de Haas, S. Sen, G. Strydom, R. Mphahlele, B. Tyobeka, V. Seker, H.D. Gougar, H.C. Lee, "PBMR couple neutronics/thermal hydraulics transient benchmark the PBMR-400 core design," Technical Report, Nuclear Energy Agency, Organization for Economic Co-operation and Development, Jun. 2007.

[8] Humphries, L. L., et al., MELCOR Computer Code Manuals: Volume 1; Reference Manual - Version 2.2.18019, Sandia National Laboratories, SAND2019-13442, Jan 2021.

[9] Pieter J Venter, Mark N Mitchell, Fred Fortier, "PBMR Reactor Design and Development," 18th International Conference on Structural Mechanics in Reactor Technology (SMiRT 18), Beijing, China, August 7-12, 2005, SMiRT18- S02-2.

[10] "Mechanistic Source Terms White Paper," Idaho National Lab, INL/EXT-10-17997, Rev. 0, July 2010.

[11] "State-of-the-Art Reactor Consequence Analysis Project Volume 2: Surry Integrated Analysis." U.S. Nuclear Regulatory Commission, NUREG/CR-7110, Volume 2, Rev. 1, January 2012.

[12] Lew Lommers "HTGR Technology Course for the Nuclear Regulatory Commission," May 24-27, 2010, HTR Training Course Module 10d, AREVA, available from https://art.inl.gov/NGNP/Training%20Modules%20%20HTGR%20Fundamentals/Module%2010d%20-%20RCCS.pdf.

[13] Louie, D. L., Humphries, L. L., "NSRD-10: Leak Path Factor Guidance Using MELCOR," Sandia National Laboratories, SAND2017-3200, March 2017.

[14] ASHRAE, "Handbook of Fundamentals," American Society of Heating, Refrigerating and Air-Conditioning Engineers, Inc, 1997.

[15] R.N. Morris, et al., " TRISO-Coated Particle Fuel Phenomenon Identification and Ranking Tables (PIRTs) for Fission Product Transport Due to Manufacturing, Operations, and Accidents," NUREG/CR-6844, Vol.1, U.S. Nuclear Regulatory Commission, Washington, DC (2004).

[16] "Fuel performance and fission product behavior in gas cooled reactors," IAEA TEDOC-0978, November 1997.

[17] R.O. Gauntt, "Synthesis of VERCORS and Phebus Data in Severe Accident Codes and Applications", SAND 2010-1633, Sandia National Laboratories, Albuquerque, NM, April 2010.

[18] P. W. Humrickhouse, "HTGR Dust Safety Issues and Needs for Research and Development," INL/EXT-11-21097, Idaho National Laboratory, June 2011.

[19] Miller, G. K., Petti, D. A., Maki, J. T., Knudson, D. L., Skerjanc, W. F., "PARFUME Theory and Model Basis Report," Idaho National Laboratory, INL/EXT-18-14497, September 2018

[20] El-Genk, M. S., and Tournier, J. P., "A Point Kinetics Model for Dynamic Simulations of Next Generation Nuclear Reactor," Progress in Nuclear Energy, Volume 92, September 2016, pp. 91-103.

[21] MacDonald, P.E., et al., NGNP Preliminary Point Design – Results of the Initial Neutronics and Thermal-Hydraulic Assessments during FY-2003, Idaho National Laboratory, Report No. INEEL/EXT 03 00870, Revision 1, September 2003.

[22] Bostelmann, F., et al., "SCALE Capabilities for High Temperature Gas-Cooled Reactor Analysis," Annals of Nuclear Energy, Vol. 147, 107673, November 2020.

[23] Ball, S. J., and Fisher, S. E., Next Generation Nuclear Plant Phenomena Identification and Ranking Tables (PIRTs) Volume 1: Main Report, Oak Ridge National Laboratory, NUREG/CR 6944, Vol. 1; ORNL/TM-2007/147, Vol. 1, March 2008.

[24] Seker, V. and Downar, T. J., "Reactor Analysis with PARCS/AGREE," February 24th, 2009, NRC Adams Ascension Number ML09106017, https://www.nrc.gov/docs/ML0910/ML091060017.pdf.

[25] Collin, B. P., "Diffusivities of Ag, Cs, Sr, and Kr in TRISO Fuel Particles and Graphite," Idaho National Laboratory, INL/EXT-16-39548, Revision 0, September 2016.

[26] Dwaraknath, S. S., and Was, G. S., "The diffusion of cesium, strontium, and europium in silicon carbide," Journal of Nuclear Materials, Vol. 476, pg. 155-167, 2016.

[27] Dwaraknath, S. S., and Was, G. S., "Radiation enhanced diffusion of cesium, strontium, and europium in silicon carbide," Journal of Nuclear Materials, Vol. 474, pg. 76-87, 2016.

[28] Moormann, R., "A safety re-evaluation of the AVR pebble bed reactor operation and its consequences for future HTR concepts," Forschungszentrum Jülich GmbH, Institute of Energy Research, Jül-4275, https://inis.iaea.org/collection/NCLCollectionStore/_Public/39/099/39099096.pdf.

[29] Kugeler, K., Zhang, Z., Modular High-temperature Gas-cooled Reactor Power Plant, Springer-Verlag Berlin Heidelberg, 2019.

APPENDIX A. CESIUM DIFFUSION DURING NORMAL OPERATIONS

While using MELCOR Revision 20811 for the new ATWS calculation, it was observed that the accelerated steady state diffusion results gave larger radionuclide releases from the TRISO pebbles to the coolant, especially for cesium and silver.[2] The source of the difference was traced to an update to the accelerated steady-state diffusion model. The ATWS and the DLOFC accelerated steady-state diffusivity calculations were specified to be 900 days, which corresponds to the approximate amount of time to achieve an equilibrium core. As described in Section 3.5, the accelerated steady-state calculates the long-term normal operational releases from the TRISO pebbles to the coolant. An update to the accelerated steady-state scaling was introduced after Revision 19798, which led to the higher steady-state releases.

It was concluded that use of the IAEA diffusivity values from Table 3-5 for intact TRISO particles is likely conservative at normal operating temperatures, as discussed below. It is difficult and expensive to experimentally measure the diffusivity of fission products through the various TRISO layers. Consequently, there are limited data and most data with irradiated TRISO dates to the German AVR program. The different results in Reference [16] show an order of magnitude variations in the measured diffusivities. Similarly, a more recent compilation of TRISO diffusivities in Reference [25] generally cites much of the same data and illustrates the scatter from the various sources.

While all the TRISO layers offer resistance to fission product release, the silicon carbide layer is the most important for cesium diffusivity. The silicon carbide layer is important at high temperatures but also the limiting layer at normal operating temperatures. The peak and average TRISO fuel temperatures during the MELCOR steady state are 1266 K and 1091 K, or 7.8 and 9.2, respectively, as also shown on Figure A-1. The temperature profile across the TRISO layers during the accelerated steady state varies by location in the core as indicated on the figure. The minimum fuel temperature is 792 K (i.e., 12.6 on Figure A-1), which is beyond the right side of the graph, as indicated by the line segment above the diffusivity curves. The TRISO layer diffusivities are calculated based on the fuel temperature at each node in the core.

Figure A-2 shows an assortment of cesium diffusivity correlations through the silicon carbide layer, which are also summarized in Table A-1. All the calculations in Sections 4.1, 4.2, and 4.3 used the cesium silicon carbide layer diffusivity labeled IAEA FRG (demo calcs). It was developed by a German researcher using AVR data. As presented in the IAEA reference [16], the IAEA FRG correlation has two-parts (i.e., see the formula in Table 3-5). However, all calculations in Sections 4.1 and 4.2 only used the low temperature portion of the diffusivity correlation due to a code limitation in Revision 19798. As shown in Figure A-2 with the IAEA FRG (2-part) curve, the second part of the diffusivity correlation is important when 10,000/T is greater than 6 (i.e., greater than 1666 K/1392°C).

Reference [25] includes recommended diffusivity correlations. Reference 23 states that the IAEA FRG (2- part) correlation is the one recommended by German researchers. Reference [25] states that the Myers lower- and upper-limit correlations are the consensus recommendation by United States TRISO research programs.

---

[2] The cesium release fraction changed from 1.5×10^{-9} to 5.8×10^{-4}. The magnitude of the silver release increased from 6.0×10^{-8} to 3.9×10^{-3}. In contrast, the updated fractional strontium, krypton, and iodine releases were higher but still with a very low magnitude (i.e., $< 4 \times 10^{-7}$).

The IAEA FRG and Myers correlations show about a factor of 10 difference at low temperatures that has an impact on the steady-state cesium release from the TRISO pebbles. Table A-1 indicates the results of the accelerated steady-state cesium release from the TRISO pebbles. Before the updates to the accelerated steady-state diffusion solution, MELCOR Revision 19798 predicted a fractional cesium release of 1.5×10^{-9} (i.e., fraction of the initial inventory). The updated release is 5.8×10^{-4}. Since the steady-state temperatures are below any diffusivity variation at higher temperature captured in the IAEA FRG 2-part diffusivity formulation, the one-part and two-part updated results using MELCOR Revision 20811 were nearly identical (see Table A-1). Similarly, the Myers lower- and upper-limit correlation results were identical and predicted an accelerated steady state fractional cesium release of 3.1×10^{-3}. Both the updated IAEA FRG and the Myers values are larger than the results from the demo calculations, which was 1.5×10^{-9}.

While some variation in the accelerated cesium release was expected due to the MELCOR code updates, the relatively large magnitude of the updated cesium release after the accelerated steady state was not expected. To further investigate the relative magnitude of the updated results, some new calculations and related references were reviewed with focus on cesium releases. The results of the investigation are discussed next.

Two recent articles by Dwaraknath [26][27] on the diffusivity through the carbon silicon layer identify grain boundary diffusion as being dominant mechanism at lower temperatures (i.e., operating temperatures for the PBMR-400). In contrast, thermal bulk diffusion is dominant at higher temperatures (i.e., accident conditions for PBMR-400). Reference [27] identifies radiation damage of the silicon carbide layer as having an effect on the magnitude of the diffusivity. In particular, the radiation damage enhanced diffusivity (RED) through the grain boundary (GB) was the dominate contributor to the overall diffusivity at low temperature. The radiation damage enhanced GB diffusion is essentially independent of temperature whereas bulk thermal diffusion increases with temperature. As the TRISO particle coating temperature increases, bulk diffusion exceeds GB diffusion and becomes the dominant diffusion mechanism.

The data and two example correlations using the results from Dwaraknath [27] are shown in Figure A-2 and Table A-1. The investigators developed the correlations by putting a temperature-independent fit through Dwaraknath's bulk and GB neutron RED data from Figure 12 in Reference [27]. The low-temperature Dwaraknath data was added to the second part of the Myers lower limit correlation. When the Dwaraknath bulk diffusion model is used, the accelerated steady-state fractional cesium release is 8.9×10^{-9}. However, the GB model gives a result of 8.7×10^{-4}, which is consistent with the IAEA FRG and Myers results. Dwaraknath explains that bulk and GB diffusion are occurring simultaneously at low temperatures but GB diffusion is dominant, as illustrated by the MELCOR predictions in Table A-1.

In Reference [26], Dwaraknath demonstrates a new technique that maintains a thin film geometry to allow the use of depth profiling techniques without causing radiation damage in the SiC. He suggested that historical data and correlations found in the IAEA summary report [16] were too high because there was an inadvertent inclusion of failed TRISO or lower quality TRISO in the measurements. The Dwaraknath data agreed well with lower temperature data from Nabielek and Myers, which is described as having the highest quality TRISO particles with the lowest defect fraction. Reference [26] concluded that the actual diffusivity is lower than the often-cited German or Myers correlations.

In Reference [27], Dwaraknath included the impact of radiation damage to the silicon carbide layer on diffusivity. When enhanced diffusion due to radiation damage (i.e., RED) is included, the grain

boundary diffusion due to defects from radiation damage is dominant at lower temperatures and approximately independent of temperature. As shown in Figure A-2, the GB RED diffusion is higher than the bulk diffusion rate. The impact of the higher GB RED diffusion rate on the MELCOR predictions was significant relative to Dwaraknath's bulk diffusion-only result but within the range of results from the IAEA FRG and Myers correlations (see Table A-1). Dwaraknath concluded that variations in the radiation enhanced diffusion is responsible for the variations in the historical diffusivity correlations and data (e.g., from [16]).

The observations and measurements from the German AVR provides order of magnitude insights into the long-term cesium releases from the TRISO pebbles into the coolant. Reference [28] from the research center in Jülich, Germany where the AVR operated cited cesium contamination was complicating and slowing the AVR decommissioning [28].

> *"The AVR primary circuit is heavily contaminated with metallic fission products (Sr-90, Cs-137) which create problems in current dismantling . The amount of this contamination is not exactly known, but the evaluation of fission product deposition experiments indicates that the end of life contamination reached several percent of a single core inventory, which is some orders of magnitude more than precalculated and far more than in large LWRs . A major fraction of this contamination is bound on graphitic dust and thus partly mobile in depressurization accidents, which has to be considered in safety analyses of future reactors [28]."*

Reference [28] identifies some contributing factors to the high cesium contamination and cites approximately 4 years of operation with unknown peak fuel temperatures greater than 900°C[3] (i.e., not intended but occurred due to inadequate temperature instrumentation). However, Reference [28] also notes that commercial HTGRs may have 40 yr of full power operation and may desire similar high temperature operations. The AVR experience is also complicated by use of two-layer fuel (HTI-BISO) at the beginning of its operation, which had coatings that were superior to TRISO in retaining cesium but had more coating defects.

The Reference [28] findings are collaborated by Dr. Kurt Kugeler, the former head of the research center in Jülich, Germany. Kugeler estimates that the peak Cs-137 concentration was 1.2 $x10^{13}$ Bq, which corresponds to approximately 1% of the whole core equilibrium inventory (i.e., 1.67$x10^{15}$ Bq) [29].

In summary, the long-term steady-state releases can be affected by the diffusivity correlations and the calculated core temperature profile. This appendix examines the impact of various correlations following the update to MELCOR's accelerated steady state diffusion model. The updated MELCOR predictions using the various correlations are compared to the value from the MELCOR demonstration calculations in Sections 4.1 and 4.2. The updated version of MELCOR corrected the steady state release model and added provisions for a 2-part diffusivity correlation. The MELCOR-predicted steady-state cesium releases over 900 days of operation range from 0.3% using the Myers correlation from Reference [25] to 0.06% using the 2-part IAEA FRG correlation [16]. These values were larger than the 1.5$x10^{-7}$% value from the demonstration calculations. However, the German AVR also experienced a larger cesium release during normal operations.

The TRISO radionuclide diffusivities and manufacturing quality is an active research area that has uncertainties and lack of data. This appendix illustrates MELCOR's capabilities to explore these uncertainties. While this appendix explored cesium diffusivity uncertainty, the uncertainty or lack of

---

[3] Note, the PBMR-400 design exit gas temperature is 900°C, and MELCOR-predicted peak fuel temperature during operation is 993°C.

data for the other radionuclides (e.g., iodine) may also need similar considerations. Until better data are available, uncertainty evaluations can be used to better characterize the range of outcomes and to help sort out the most significant parameters impacting the predictions. MELCOR includes flexible modeling features for such uncertainty modeling.

Table A-1 Accelerated steady state release of cesium from the pebbles.

Diffusivity model	Diffusivity correlation (m^2/s)	Accelerated steady state release (faction of initial inventory)	Code Version
Demo calculations in Sections 4.1, 4.2	$D = 7.2^{-14} \exp\left(\frac{125{,}000}{RT}\right)$	1.5x10^{-9}	Rev 19798 *
IAEA FRG (demo calcs) [16][25]	$D = 7.2^{-14} \exp\left(\frac{125{,}000}{RT}\right)$	5.8x10^{-4}	Rev 20811 #
IAEA(2-part) [16]	$D = 7.2^{-14} \exp\left(\frac{125{,}000}{RT}\right) + 1.6^{-2} \exp\left(\frac{514{,}000}{RT}\right)$	5.8x10^{-4}	
Myers – lower limit [25]	$D = 6.7^{-14} \exp\left(\frac{106{,}000}{RT}\right) + 1.1^{-4} \exp\left(\frac{437{,}000}{RT}\right)$	3.1x10^{-3}	
Myers – upper limit [25]	$D = 6.7^{-14} \exp\left(\frac{106{,}000}{RT}\right) + 2.4^{-2} \exp\left(\frac{482{,}000}{RT}\right)$	3.1x10^{-3}	
Dwaraknath bulk [27] + Myers [25]	$D = 1.44^{-21} + 1.1^{-4} \exp\left(\frac{437{,}000}{RT}\right)$	8.9x10^{-9}	
Dwaraknath GB [27] + Myers [25]	$D = 2.58^{-19} + 1.1^{-4} \exp\left(\frac{437{,}000}{RT}\right)$	8.7x10^{-4}	

Note:
* Before updates to the accelerated steady state diffusion calculations.
# After updates to the accelerated steady state fission diffusion calculations.

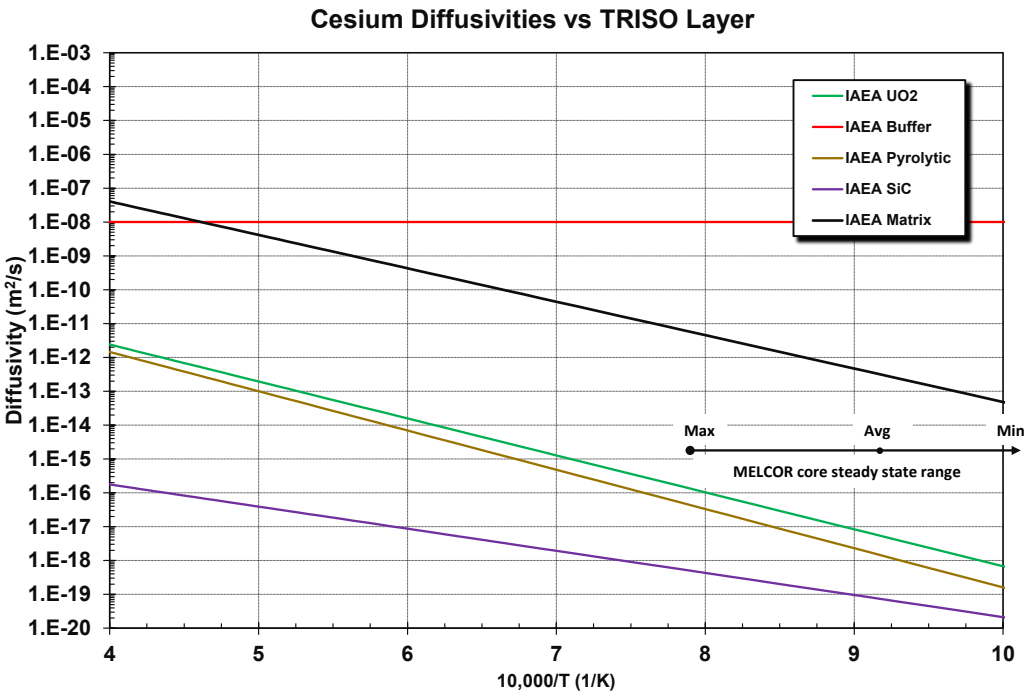

Figure A-1 Comparison of cesium diffusivities used in the demo calculations.

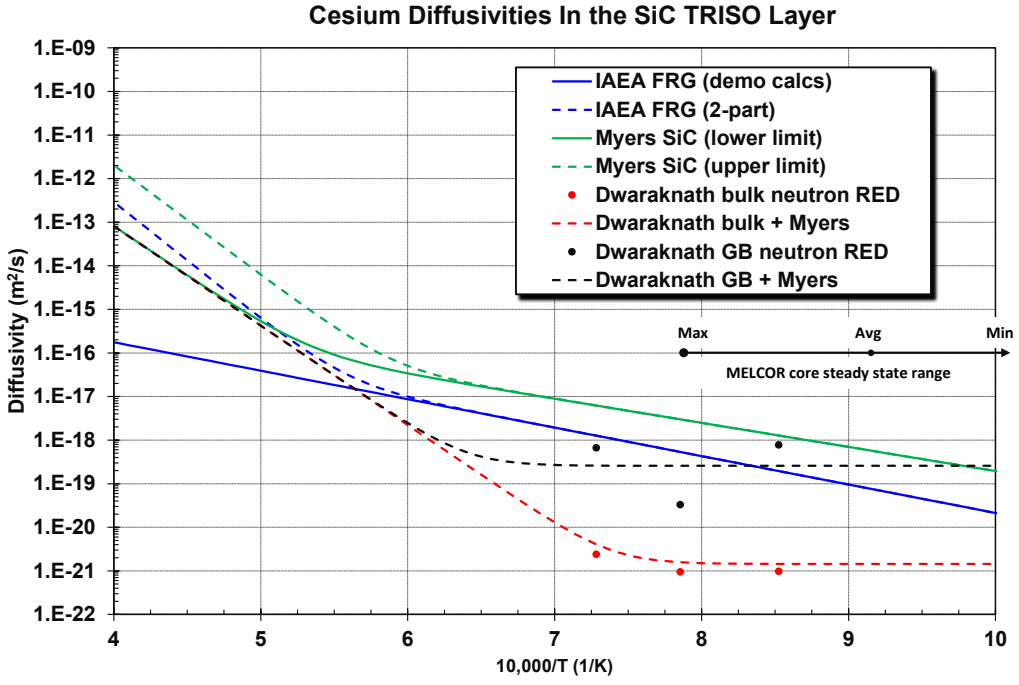

Figure A-2 Comparison of cesium diffusivities in the SiC TRISO layer.

DISTRIBUTION

Email—Internal

Name	Org.	Sandia Email Address
David Luxat	08852	dlluxat@sandia.gov
Brad Beeny	08852	babeeny@sandia.gov
Technical Library	01911	sanddocs@sandia.gov

Email—External (encrypt for OUO)

Name	Company Email Address	Company Name
Jason Schaperow	jason.schaperow@nrc.gov	NRC
Hossein Esmaili	hossein.esmaili@nrc.gov	NRC
Shawn Campbell	campbell.shawn@nrc.gov	NRC

Hardcopy—Internal

Number of Copies	Name	Org.	Mailstop

This page left blank

This page left blank

Sandia National Laboratories

Sandia National Laboratories is a multimission laboratory managed and operated by National Technology & Engineering Solutions of Sandia LLC, a wholly owned subsidiary of Honeywell International Inc. for the U.S. Department of Energy's National Nuclear Security Administration under contract DE-NA0003525.